

The spin and shape of dark matter haloes in the Millennium simulation of a Λ CDM universe

Philip Bett^{1,3}, Vincent Eke¹, Carlos S. Frenk¹, Adrian Jenkins¹, John Helly¹,
and Julio Navarro²

¹*Institute for Computational Cosmology, University of Durham, South Road, Durham, DH1 3LE, UK*

²*Department of Physics and Astronomy, University of Victoria, Victoria, BC, V8P 5C2, Canada*

³*P.E.Bett@durham.ac.uk*

2 December 2024

ABSTRACT

We investigate the spins and shapes of over a million dark matter haloes identified at $z = 0$ in the Millennium simulation. Our sample spans halo masses ranging from dwarf galaxies to rich galaxy clusters. The very large dynamic range of this Λ CDM cosmological simulation enables the distribution of spins and shapes and their variation with halo mass and environment to be characterised with unprecedented precision. We compare results for haloes identified using three different algorithms, and investigate (and remove) biases in the estimate of angular momentum introduced by both the algorithm itself and by numerical effects. We introduce a novel definition of a halo, based on the branches of the halo merger trees, which is more appropriate for comparison with real astronomical objects than the traditional “friends-of-friends” and “spherical overdensity” haloes. We find that for this many objects, the traditional lognormal function is no longer an adequate description of the distribution, $P(\lambda)$, of the dimensionless spin parameter, λ , and we provide a different function that gives a better fit. The variation of spin with halo mass is weak but detectable, although the trend depends strongly on the halo definition used. For the entire population of haloes, we find median values of $\lambda_{\text{med}} = 0.0367\text{--}0.0429$, depending on the definition of a halo. The haloes exhibit a range of shapes, with a preference for prolateness over oblateness. More massive haloes tend to be less spherical and more prolate. We find that the more spherical haloes have less coherent rotation in the median, and those closest to spherical have a spin independent of mass ($\lambda_{\text{med}} \approx 0.033$). The most massive have a spin independent of shape ($\lambda_{\text{med}} \approx 0.032$). The majority of haloes have their angular momentum vector aligned with their minor axis and perpendicular to their major axis. We find a general trend for higher spin haloes to be more clustered, with a stronger effect for more massive haloes, which for galaxy cluster haloes can be larger than a factor of ~ 2 .

Key words: cosmology: dark matter – galaxies: haloes – methods: N -body simulations

1 INTRODUCTION

The formation of galaxies is intimately linked to the acquisition and distribution of angular momentum. In the current cosmological paradigm, the inflationary Λ CDM model, cosmic structures grow hierarchically. Dark matter haloes form by the dissipationless gravitational collapse of material associated with peaks in the primordial density fluctuation field, growing, through mergers and smooth accretion, into objects with a wide range of masses at the present day. Galaxies form when baryons cool and condense near the centre of these haloes (White & Rees 1978, White & Frenk

(1991). They undergo mergers and tidal interactions along with their haloes, giving rise to the rich spectrum of galaxy types and environments that we see today.

Understanding the generation and evolution of the angular momentum of dark matter haloes is a prerequisite for understanding the angular momentum and morphology of galaxies. For example, the distribution of halo spins is a basic input to models of galaxy formation (e.g. Mo et al. 1998, van den Bosch 1998, Cole et al. 2000). The early evolution of the angular momentum of a density perturbation is adequately described by the linear tidal torque theory (see e.g. Hoyle 1949, Peebles 1969, Doroshkevich 1970, White

1984, Catelan & Theuns 1996, Lee & Pen 2000). However, as work such as that of White (1984) and Porciani et al. (2002) has shown, the non-linear effects inherent in the formation of large-scale structure lead to large quantitative disagreements between the predictions of the tidal torque theory and the angular momenta found in N -body simulations of dark matter haloes.

N -body simulations provide the way to progress beyond the linear regime. As computing power has improved, so has the scale and resolution of simulations. Very early numerical studies of the angular momentum of “proto-galaxies” were performed by Peebles (1971) (with $N_p \sim 100$ particles) and Efstathiou & Jones (1979) ($N_p = 1000$), and led the way to the analysis of the spins and shapes of CDM haloes in more sophisticated simulations (Davis et al. 1985; Barnes & Efstathiou 1987; Frenk et al. 1988; all with $N_p = 32\,768$). Warren et al. (1992) used a much larger simulation ($N_p \sim 10^6$) and focused particularly on the details of the distributions of halo spins and shapes, and their relationship through the alignment of the halo angular momentum vector. Cole & Lacey (1996) also investigated the shapes and spins of dark matter haloes, in addition to various other aspects of halo structure.

An early study by Barnes & Efstathiou (1987) examined the relationship between the spatial clustering of haloes, as measured by the two-point correlation function, and their spin. Later, Lemson & Kauffmann (1999) examined the environmental dependence of halo properties, and found no correlations with halo spin. More recently, Faltenbacher et al. (2002) have carried out a mark correlation function analysis to investigate how spin varies with halo pair-separation. They found that neighbouring cluster pairs tend to have higher spins than the average.

Recent years have seen a large amount of work on the analysis of haloes in Λ CDM simulations. Halo shapes and their variation with mass were investigated by Bullock (2002), Kasun & Evrard (2005) and Allgood et al. (2006). In agreement with previous studies, halo spin was found to vary little, if at all, with halo mass. The relationship between halo shape and spin was investigated by Bailin & Steinmetz (2005), Shaw et al. (2005), Gottlöber & Turchaninov (2006), and Avila-Reese et al. (2005). While this paper was being completed, independent analysis of halo properties, investigating halo concentrations, spins and shapes in a series of simulations, was posted by Macciò et al. (2006).

Using the the 10-billion particle Millennium simulation of the evolution of dark matter in the Λ CDM cosmology (Springel et al. 2005), we re-examine, in this paper, some of the shape and spin properties of dark matter haloes previously considered. Our analysis improves upon earlier work because the millions of haloes that formed in this simulation provide unprecedented statistical power. This allows us, for example, to quantify the distribution of halo spins and the relationship between spin, halo mass and shape with a precision that has not hitherto been possible. Unlike previous work, we consider different ways to define and identify haloes in the simulations; it turns out that the details of halo selection can have a strong impact on the results. Finally we investigate how halo clustering depends on spin and shape for haloes of different mass.

This paper is structured as follows. Section 2 provides a description of the Millennium simulation itself, the halo

Ω_Λ	Ω_M	Ω_b	h	n	σ_8
0.75	0.25	0.045	0.73	1.00	0.9
L_{box}	N_{part}	m_p	η		
$500\,h^{-1}\text{Mpc}$	$2160^3 \approx 10^{10}$	$8.6 \times 10^8\,h^{-1}\text{M}_\odot$	$5\,h^{-1}\text{kpc}$		

Table 1. Cosmological and simulation parameters for the Millennium Run. The first row describes the cosmology used. It gives the density parameters $\Omega_i := \frac{\rho_i}{\rho_{\text{crit}}}$, where the critical density $\rho_{\text{crit}} := \frac{3H_0^2}{8\pi G}$ (with $\rho_\Lambda := \frac{\Lambda}{8\pi G}$ and $\Omega_{\text{tot}} = \Omega_\Lambda + \Omega_M = 1$), the Hubble parameter where $H_0 = 100h(\text{km s}^{-1}\text{Mpc}^{-1})$, the spectral index, n , and σ_8 , the linear-theory power spectrum variance in spheres of radius $8\,h^{-1}\text{Mpc}$. The second row gives the simulation parameters: the length of the side of the simulation cube, the number of particles, the resulting particle mass and the gravitational softening length. For further details, see Springel et al. (2005).

catalogues constructed from it, and details of various halo properties. Section 3 describes the cuts made to the catalogues to remove haloes whose properties are unreliable or biased, due to both numerical effects and the group-finding algorithms. The main results of this paper are presented in §4, where we describe the distribution of halo spins as a function of mass and shape, and examine its effect on halo clustering. Our conclusions are presented in §5. Finally, the Appendix shows various examples of haloes that illustrate the effects of the group-finders.

2 DARK MATTER HALOES IN THE MILLENNIUM SIMULATION

2.1 The simulation

The Millennium simulation is described by Springel et al. (2005). It followed the evolution of 10 billion dark matter particles in the Λ CDM model, the standard paradigm of cosmology, which is strongly favoured by measurements of the temperature anisotropies in the microwave background radiation (Spergel et al. 2003, 2006) and by measurements of the clustering of galaxies (Percival et al. 2002; Sánchez et al. 2006; Tegmark et al. 2004). For reference, the key parameters of the simulation are listed in Table 1.

2.2 The halo catalogues

2.2.1 FOF haloes

The simulation gives the position and velocity of each particle at each “snapshot” in time; 64 snapshots are stored from the initial redshift ($z = 127$) to the present, enabling redshift-dependent statistics to be studied. Part of the power of the simulation lies in its large dynamic range in the mass of objects identified within it. A ‘friends-of-friends’ group-finder (FOF, Davis et al. 1985) was run on-the-fly, while the simulation was performed, with a linking length of $s_0 = b(L_{\text{box}}^3/N_{\text{part}})^{1/3}$ where $b = 0.2$, to attempt to select virialised structures in the particle distribution. It found 17 709 121 groups containing at least 20 particles, i.e. of mass $\gtrsim 1.7 \times 10^{10}\,h^{-1}\text{M}_\odot$. The most massive group contained 4 386 162 particles ($\approx 3.8 \times 10^{15}\,h^{-1}\text{M}_\odot$). We can therefore

identify dark matter haloes over a range of more than 5 orders of magnitude in mass, ranging from subgalactic clumps to the most massive clusters.

An enhanced version of the SUBFIND (Springel et al. 2001, 2005) program was run on the data to identify self-bound substructures within each FOF halo. The SUBFIND algorithm is essentially a two-step process. The first task is to identify subhalo candidates within each FOF halo. This is done using an adaptively-smoothed dark matter density field, effectively lowering a density threshold and identifying the peaks that grow out of it. The second stage consists of performing a gravitational unbinding procedure on the candidates, successively removing particles that are not bound to the subhalo candidate. For this purpose, the potential energies are computed using a tree algorithm similar to that used for the simulation itself. The candidates that are left with at least 20 particles after this procedure are then subhaloes of the parent halo. The algorithm can and does identify subhaloes within subhaloes. It results in the FOF haloes typically consisting of a hierarchy of self-bound structures (which are not necessarily bound to each other), and a set of particles (known as “fuzz”) that are spatially linked to the halo but not bound to any structure. The most massive “subhalo” (MMSH) typically contains most of the mass of the FOF halo, and so is best regarded as the self-bound background halo itself, with the remaining subhaloes as its substructure.

In addition to finding the bound structures within haloes, SUBFIND also computes certain properties of the subhaloes, which are then stored in the subhalo catalogue files. These include the location of the potential minimum, the ID number of the most bound particle, the mass (number of particles), and the half-mass radius. SUBFIND also computes and stores additional data related to each parent halo. Starting at the potential minimum of the MMSH of a halo, three radii are found: the first two are those where the density within them drops below $200\rho_{\text{crit}}$ and $200\bar{\rho}$, to aid comparison with other work. The third is the virial radius proper, which uses the fitting formula of Bryan & Norman (1998) for spherical top-hat collapse in a flat ($\Omega_{\Lambda} + \Omega_{\text{M}} = 1$) cosmology (see also Eke et al. 1996):

$$\frac{\rho}{\rho_{\text{crit}}} = 18\pi^2 + 82(\Omega_{\text{M}}(z) - 1) - 39(\Omega_{\text{M}}(z) - 1)^2 \quad (1)$$

This gives $\rho/\rho_{\text{crit}} \approx 94$ at $z = 0$. Although these properties are associated with sets of grouped particles, SUBFIND does not restrict itself to these particles when computing them.

The first ‘cut’ made to the FOF halo catalogue is implicit in the definition of the halo properties considered here. We use the centre (potential minimum) of the MMSH as the centre of the halo itself, which means that only FOF haloes for which SUBFIND has found bound substructures are included; haloes without substructure (and hence without an MMSH) are excluded from the “raw” FOF catalogue. This has the effect of reducing the catalogue size by 12.5%, preferentially at lower masses. We will refer to this reduced set of haloes as the FOF catalogue from here on, and we will not discuss the larger raw FOF catalogue further. Table 2 gives a list of each halo catalogue, and the number of haloes they contain.

Halo catalogue	Number of haloes	
FOF (raw)	17 709 121	
FOF (base)	15 494 624	(87.5% of FOF Raw)
FOF-QE	13 287 100	(85.8% of FOF Base)
FOF-QE- N_{p}	1 332 239	(8.60% of FOF Base)
SO (base)	15 458 379	(99.8% of FOF Base)
SO-QE	14 049 411	(90.9% of SO Base)
SO-QE- N_{p}	1 239 494	(8.02% of SO Base)
TREE (base)	17 041 498	(110.0% of FOF Base)
TREE-QE	16 993 302	(99.7% of TREE Base)
TREE-QE- N_{p}	1 503 922	(8.83% of TREE Base)

Table 2. Numbers of haloes in the various halo catalogues considered in this paper. The base catalogues are discussed in §2.2, and those with quasi-equilibrium (QE) and particle number N_{p} cuts are described in §3.

2.2.2 SO haloes

The parameters found by SUBFIND make it possible to construct a second halo catalogue, in which each halo consists of only the particles within R_{vir} of the centre of the MMSH of the corresponding FOF object (note that these particles do not have to be members of the FOF halo). This will yield haloes whose definition is similar to those from a “spherical overdensity” algorithm (Lacey & Cole 1994), so we will refer to them as the SO halo catalogue. We do not impose a lower limit on the number of particles comprising these SO haloes; as a result, haloes are identified with masses $< 20m_{\text{p}}$ when their virial radii encompass fewer particles than their original FOF halo. This is simply a consequence of the algorithm employed; later examination of halo spins reveals the need for a much higher particle-number limit, as discussed in full in Section 3. This halo definition is similar, but not identical, to that used in Macciò et al. (2006).

2.2.3 TREE haloes

As a third definition of haloes, we use the ‘merger-tree’ haloes described by Harker et al. (2005). These are the $z = 0$ objects in a catalogue of merger trees constructed in the Millennium Run (Helly et al., in preparation). These merger trees are similar to, but distinct from those of Springel et al. (2005) and Gao et al. (2005), who used different criteria for identifying and tracking the haloes over time. The merger-tree-halo catalogue used here was designed with the needs of the N -body GALFORM semi-analytic models in mind (e.g. Helly et al. 2003, Bower et al. 2005). The haloes in this catalogue are formed from the SUBFIND-processed FOF haloes in the following way. Each halo is initially taken to consist solely of its constituent subhaloes (i.e., it is the corresponding FOF halo but without the fuzz). Next, a “splitting” algorithm is applied, which attempts to account for the linking of distinct bound objects that often occurs with FOF. A subhalo can be split off from its parent halo if it satisfies at least one of the following conditions: 1) The distance between the subhalo’s centre and the parent’s centre is more than twice the parent’s half-mass radius; or 2) the halo has retained at least 75% of the mass it had at the last

output in which it was an independent halo. This second condition is based on the idea that if the subhalo really was merging with the halo, it would rapidly be stripped of mass, but if it was just a rapid encounter causing an artificial link then its mass would be retained. If the subhalo is split off, any other subhaloes that reside within twice its half-mass radius are also split off to become part of the new halo. We shall refer to haloes defined in this method as the TREE haloes.

2.3 Halo properties

This work concentrates on the dimensionless spin parameter λ introduced by Peebles (1969, 1971). This is defined as:

$$\lambda := \frac{J|E|^{1/2}}{GM_h^{5/2}} \equiv \frac{j|E|^{1/2}}{GM_h^{3/2}} \quad (2)$$

where M_h is the halo mass, J is the magnitude of the angular momentum vector (and j is the specific angular momentum), E is the total energy, and G is Newton's gravitational constant. The spin parameter is a measure of the amount of coherent rotation in a system compared to random motions. For a spherical object, it is approximately the ratio of its own angular velocity to the angular velocity needed for it to be supported against gravity solely by rotation (see e.g. Padmanabhan 1993).

The specific angular momentum \mathbf{j} and kinetic energy T of each halo containing N_p particles are given by:

$$\mathbf{j} = \frac{1}{N_p} \sum_{i=1}^{N_p} \mathbf{r}_i \times \mathbf{v}_i \quad (3)$$

$$T = \frac{1}{2} M_h \sum_{i=1}^{N_p} \mathbf{v}_i^2 \quad (4)$$

where \mathbf{r}_i is the position vector of particle i relative to the halo centre, and \mathbf{v}_i is its velocity relative to the halo centre of momentum.

The halo potential energy, U , is calculated using all halo particles if $M_h \leq 1000m_p$, and is rescaled up from that of 1000 randomly-sampled particles otherwise. The potential is that used in the simulation itself:

$$U = \left(\frac{N_p^2 - N_{\text{sel}}}{N_{\text{sel}}^2 - N_{\text{sel}}} \right) \left(\frac{-Gm_p^2}{\eta} \right) \sum_{i=1}^{N_{\text{sel}}-1} \sum_{j=i+1}^{N_{\text{sel}}} -W_2(r_{ij}/\eta) \quad (5)$$

where N_{sel} is the number of selected particles ($N_{\text{sel}} \leq 1000$), η is the softening length (see Table 1), r_{ij} is the magnitude of the separation vector between the i th and j th particles in the halo, and the softening kernel (see Springel et al. 2001) is:

$$W_2(u) = \begin{cases} \frac{16}{3}u^2 - \frac{48}{5}u^4 + \frac{32}{5}u^5 - \frac{14}{5}, & 0 \leq u \leq \frac{1}{2}, \\ \frac{1}{15u} + \frac{32}{3}u^2 - 16u^3 + \frac{48}{5}u^4, & \frac{1}{2} \leq u \leq 1, \\ -\frac{1}{u}, & u \geq 1 \end{cases} \quad (6)$$

A halo's shape is derived from its mass distribution, which we characterise using the inertia tensor, \mathbf{I} . This relates angular momentum \mathbf{J} and angular velocity $\boldsymbol{\omega}$ through $\mathbf{J} = \mathbf{I}\boldsymbol{\omega}$, and is formed from the following components:

$$I_{\alpha\beta} := \sum_{i=1}^{N_p} m_i (\mathbf{r}_i^2 \delta_{\alpha\beta} - r_{i,\alpha} r_{i,\beta}) \quad (7)$$

where \mathbf{r}_i is the position vector of the i th particle, α and β are the tensor indices with values of 1, 2 or 3, and $\delta_{\alpha\beta}$ is the Kronecker delta. The process of diagonalising \mathbf{I} is equivalent to rotating the coordinate system to find a set of axes in which a torque about one does not induce a rotation about another; i.e. such that \mathbf{J} is parallel to $\boldsymbol{\omega}$. These axes then describe a hypothetical uniform ellipsoid whose axes $a \geq b \geq c$ are those of the halo itself:

$$\mathbf{I} = \frac{1}{5} M_h \begin{pmatrix} b^2 + c^2 & 0 & 0 \\ 0 & a^2 + c^2 & 0 \\ 0 & 0 & a^2 + b^2 \end{pmatrix} \quad (8)$$

The eigenvalues are the moments of inertia for rotation about that axis. For example, rotation about the semimajor axis \mathbf{a} has the moment of inertia $\mathcal{I}_a = \frac{1}{5} M_h (b^2 + c^2)$; note that $\mathcal{I}_a \leq \mathcal{I}_b \leq \mathcal{I}_c$. These eigenvalues can then be combined to find the relative axis lengths, e.g.

$$a = \sqrt{\frac{5}{2M_h} (-\mathcal{I}_a + \mathcal{I}_b + \mathcal{I}_c)} \quad (9)$$

The axis vectors are given directly by the corresponding eigenvectors, so that, for example, rotation about the \mathbf{a} -axis of the ellipse (with the longest length a) has the smallest moment of inertia, \mathcal{I}_a .

Much of the literature on halo shapes uses the following description of the mass distribution, confusingly also calling it the inertia tensor (see, e.g. Cole & Lacey 1996, Hopkins et al. 2005, Bailin & Steinmetz 2005, Shaw et al. 2005):

$$\mathcal{M}_{\alpha\beta} = \frac{1}{N_p} \sum_{i=1}^{N_p} r_{i,\alpha} r_{i,\beta} \quad (10)$$

The results are entirely equivalent: if one diagonalises this matrix, then a , b and c can be found as just the square roots of the eigenvalues, and the eigenvectors again give the axis vectors.

Once the halo's principal axes have been found, relationships between the axes and between the shape and other properties such as spin can be examined in terms of the axis ratios $p := c/b$, $q := b/a$ and $s := c/a$. The minor-to-major axis ratio s is a useful measure of the sphericity of the system, but does not specify in what way a halo might be aspherical. For this, we can use the triaxiality parameter introduced by Franx et al. (1991):

$$\mathcal{T} = \frac{a^2 - b^2}{a^2 - c^2} \quad (11)$$

This measures whether a halo is prolate ($\mathcal{T} = 1$) or oblate ($\mathcal{T} = 0$), but it does not quantify how aspherical a halo is.

3 CLEANING THE HALO CATALOGUES

The raw spin distribution of all FOF haloes is shown in Fig. 1. It shows a feature not usually seen in other published spin distributions (e.g. Gardner 2001, Avila-Reese et al. 2005, Tonini et al. 2006, among many others), namely a long tail at higher spins; there are 900 748 objects with spin $\lambda \geq 0.3$. Fig. 2 shows the spin distribution as a function of halo

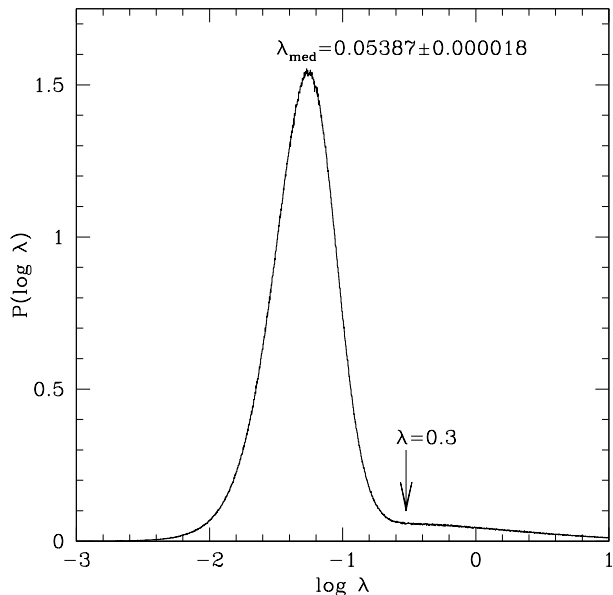


Figure 1. Histogram of the spin parameter of all FOF haloes in the Millennium Run, showing a long tail to high spins. The tail continues up to $\lambda \approx 680$, and there are over 900 000 objects with $\lambda \geq 0.3$ (marked on the graph). The median spin of the distribution, λ_{med} , is displayed with the uncertainty given by Eqn. 12.

mass, rescaled to show the fractional number of objects at each mass so the trend of the mass function is removed. It shows that the high-spin tail comes from objects over a large range of masses. Just looking at Figs. 1 and 2 by eye suggests that there is an entire class of objects whose spin distribution differs from the lognormal function usually seen in other work. Furthermore, the spin medians over mass bins show a strong upturn towards lower halo mass (see Fig. 4). We investigate the causes of these effects, and characterise the objects involved. We can then attempt to remove them from the catalogues, leaving a sample of objects that we can use to describe the spin distribution of ‘typical’ haloes. It is important to note that these peculiarities in the spin distribution only become noticeable when analysing a large number of haloes over a wide range of masses, such as is possible with the Millennium Run.

3.1 Examining the problem: groupfinder effects

Examining the data for the haloes with these presumed-anomalous high spins shows that the major contributing factors are their kinetic energies, T . The objects all have anomalously high velocity dispersions, and this is due to the way each halo is defined in relation to its environment. There are various specific common situations that illustrate the ways this can come about in haloes over such a wide range of masses.

Well-resolved objects identified using the FOF algorithm are often at risk of becoming linked with neighbouring objects via tenuous bridges of particles. Low-mass particle bridges are usually extremely transient structures, being just a chance grouping of particles at that instant in time. The joining of two (or more) otherwise unrelated objects of

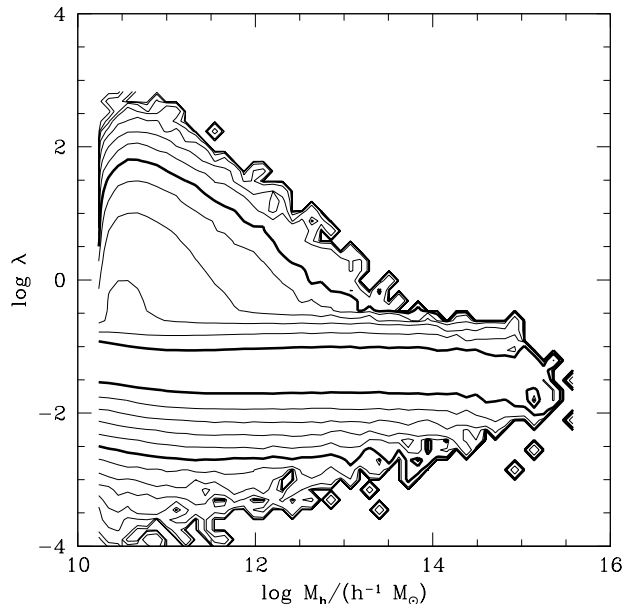


Figure 2. Halo spin as a function of halo mass for all FOF haloes. The contours indicate the relative number density of haloes with that value of $\lambda(M_h)$; that is, the haloes were binned onto a 50×50 grid between the maximum and minimum values in $\log M_h$ and $\log \lambda$, and the number of haloes in each grid cell was normalised by the number of haloes in that mass-bin, thus removing the effects of the halo mass function from the plot. The contours are spaced logarithmically, with one contour for every factor of $10^{0.5}$ in halo number density. The innermost bold contour represents 10^{-1} (i.e. a tenth of the haloes in each mass bin), and the outer bold contour represents $10^{-3.5}$. Notice the high-spin bulge, which extends over a large range of halo masses. The results for SO haloes show a very similar distribution.

similar mass in this way results in a very large velocity dispersion and a signature of the multiple-object nature of the halo which is clearly visible in velocity-space. An example of a halo formed from objects joined by a tenuous bridge can be seen in Fig. A1.

Sometimes more massive haloes can be formed by the chaining together of somewhat smaller objects that are undergoing mergers or close flybys with their neighbours. Their multi-object composition can again be seen in velocity space as well as in real space, and although their connections are likely to be less transitory than in the case of a thin bridge, these objects are nevertheless well out of their equilibrium state, and so are unhelpful when trying to characterise the spins of typical dark matter haloes. See Fig. A2 for an example of a larger multi-object halo.

A similar effect is that of velocity contamination of small objects due to their proximity to more massive ones (see Fig. A3 for an example). Just as particles can form a bridge between passing haloes at the moment of the snapshot, so an individual particle orbit can take it within the linking length of a neighbouring halo, without forming enough of a bridge for the haloes themselves to be joined. The smaller halo will be contaminated by these interloper particles, which will have a quite different mean velocity to the halo’s own particles. This causes the mean to be shifted away from that of the ‘original’ halo, and the resulting halo

to have a much larger velocity dispersion than expected for an object of that mass. The massive neighbouring object will have a much higher velocity dispersion anyway, so will be unaffected by such effects.

These problems do not affect just the FOF haloes however. Since the SO catalogue just uses spheres grown from the MMSH of the FOF haloes, it is also very easy for them to sample the multiple velocity dispersions of linked FOF objects. Furthermore, for a larger, elongated linked FOF object, the SO group constructed from its centre will often have a strange shape, giving it a distinctly artificial appearance. (see Fig. A4 for an example). Similarly, it is just as easy for a small SO halo to be contaminated by stray particles from larger neighbours as it is for a FOF halo.

The definition of the merger tree haloes used in the TREE catalogue alleviates these groupfinder-based problems somewhat. The unbound particles excluded from the tree haloes have, by definition, higher velocities than the bound structures in the haloes. Their removal therefore reveals the more relaxed underlying haloes, with lower kinetic energies and hence λ . ‘Interloper particle’ contamination, in particular, is reduced by this feature. The halo splitting algorithm also helps in many cases by separating objects that have been spuriously linked by bridges. The base tree-halo spin-mass distribution can be seen in Fig. 3; although some of the high-spin objects remain, the majority are now gone. Investigating the remaining high-spin objects reveals them to be victims of velocity contamination from very massive neighbours. They are somewhat special cases however: for them not to have been rejected as fuzz, the contaminants must be self-bound bodies, with ≥ 20 particles each. They must also be built on density maxima independent of that of the host halo, in order for SUBFIND to have identified them as separate subhaloes. Furthermore, the interloping subhalo must be within twice the half-mass radius of the halo, so that the tree algorithm does not split it off. A consequence of this is that the resulting halo must consist of at least 40 particles, and this can be seen in the offset low-mass cutoff for high- λ haloes in Fig. 3.

For convenience, we shall refer to haloes suffering from the problems described in this subsection as ‘mis-defined’ haloes, as their anomalously-high spins originate in their definition by the groupfinder algorithm rather than any physical or numerical effect.

3.2 Examining the problem: numerical effects

The second peculiarity of the spin distributions mentioned above, the upturn in $\lambda_{\text{med}}(M_h)$ at low masses, turns out to be unrelated to the velocity contamination effects of the mis-defined haloes, and instead comes from the mass resolution of the simulation affecting the angular momenta. This effect has been seen before, for example by Reed et al. (2005) in the context of subhaloes. Consider a continuous object with angular momentum \mathbf{J}_{true} . If we construct a realisation of this object using a sample of N discrete particles, the resulting angular momentum can be modelled as the vector sum of the ‘true’ angular momentum (from the continuous object) with a noise vector oriented in a random direction: $\mathbf{J} = \mathbf{J}_{\text{true}} + \mathbf{J}_{\text{noise}}$. This will act to push the measured magnitude J up above J_{true} because the random direction of $\mathbf{J}_{\text{noise}}$ will mean it reaches outside the sphere of radius

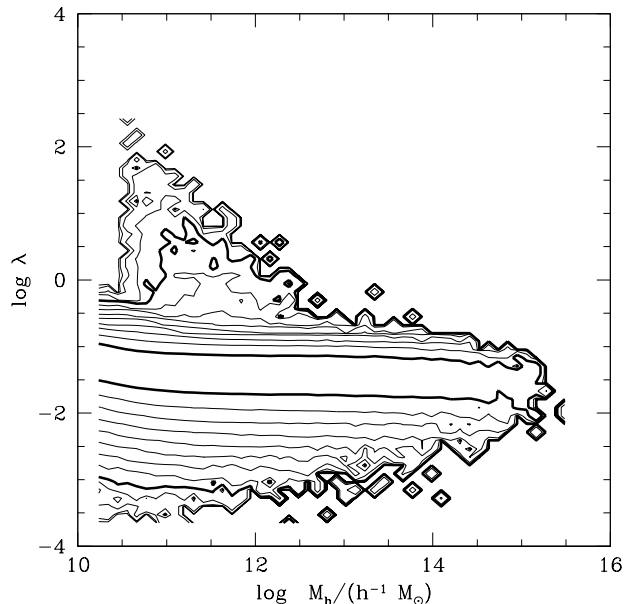


Figure 3. Spin as a function of halo mass for all TREE haloes. The contouring is as in Fig. 2, i.e. in equal logarithmic steps of $10^{0.5}$, normalised to remove the mass function. In this plot, the inner bold contour represents 10^{-1} of the haloes at each mass, and the outer bold contour represents 10^{-5} of the haloes at each mass. The merger-tree halo definition has moved many of the high-spin haloes visible in Fig. 2 down into the main body of the distribution.

$|\mathbf{J}_{\text{true}}|$ more than 50% of the time. Therefore, the random noise inherent in using discrete particles to sample a near-continuous object such as a dark matter halo would act to bias J and hence λ upwards.

Modern N -body codes such as the L-GADGET-II code used for the Millennium Run are very good at conserving quantities such as energy and angular momentum, so for a well-resolved object there is negligible inaccuracy arising from particle discreteness. For a less well-resolved object however, the effect can still be relevant, even though the angular momentum of the particles making up the halo has been well conserved. Discreteness mainly affects the outer parts of a halo, making the effective surface more jagged than that of the continuous object it represents. We also expect the outer parts to harbour most of the angular momentum. For lower-mass haloes, a greater fraction of their particles make up these ‘surface’ regions, so this problem has a greater effect; the inclusion of a single particle can make a significant contribution to λ . Hence, the spin parameter rises for haloes with fewer particles because the discreteness of the haloes’ surface layers adds noise to their ‘true’ angular momenta. (This is not the same effect as discussed in Shaw et al. (2005); there, a surface pressure term is added to the virial theorem to account for their halo truncation at R_{vir} .)

The importance of the noise contribution to λ can be examined by determining the spin distribution of the same simulation (same code and same corresponding initial condition waves) but ran at a different resolution. We performed a lower resolution resimulation of the Millennium Run, with $2160^3/64 = 540^3$ particles (so their

mass is $m_{p,low} = 64m_{p,Millen}$), which we will refer to as **milli_lowres**. The FOF and SUBFIND algorithms were implemented on **milli_lowres** in the same way as in the Millennium Run itself. Fig. 4 shows the median spin $\lambda_{med}(N_p)$ for FOF haloes in the Millennium Run and **milli_lowres**, with vertical errorbars showing a Gaussian-like estimate of the precision of the median given by:

$$\epsilon_{med} := \frac{(\lambda_{84} - \lambda_{16})}{\sqrt{N_{halo}}} \quad (12)$$

where λ_i is the i th percentile of λ ($84\% - 16\% = 68\%$, the amount of data within $\pm 1\sigma$ of a Gaussian peak) and N_{halo} is the number of haloes in that mass bin. Note that the *spread* in λ is much greater than the uncertainty in λ_{med} ; compare the errorbars in Fig. 4 with the data shown in Fig. 2.

Although the two curves show the same qualitative behaviour (the low- N_p upturn), there is a vertical shift between them. This is due to **milli_lowres** containing fewer of the mis-defined objects described in Section 3.1 than the Millennium Run itself. Decreasing the resolution effectively smooths the density field, so that small objects with more massive neighbours can disappear completely, whereas a more isolated object of the same mass may still survive (although containing fewer particles). This means that the “real” objects are retained (and there are still many under-resolved ones causing the upturn in $\lambda_{med}(N_p)$), but there is a reduction in the number of mis-defined objects. The **milli_lowres** results seem to confirm the dominance of numerical effects at low- N_p , above which the effect of noise is negligible. This is fully demonstrated in Section 3.3 where we discuss how to exclude haloes that are strongly affected by this problem.

3.3 Halo selection criteria

A relatively simple way of culling the anomalous spin objects is to remove those that are clearly out of equilibrium at the moment of the snapshot. This is not quite the same as selecting only objects that are within a certain degree of true virialisation, since that would require more dynamical information than is available: just as an object can appear to be linked to another by a bridge that may exist only fleetingly, so a halo could instantaneously have a very similar energy configuration to the time-averaged energies of a virialised object. Therefore we will apply a cut in the instantaneous ‘virial ratio’ of halo energies, $2T/U + 1$, and describe the objects that meet this criterion as haloes in a *quasi-equilibrium* (QE) state. This name avoids implying the time-averaging appropriate to the true virial ratio. The question of where to make a cut in ‘virialisation’ (i.e. applying a QE limit) is a difficult one, because the decision will always be somewhat arbitrary. Since it is desirable to minimize the effect of such arbitrariness, we chose to concentrate on the TREE haloes, since the merger-tree algorithm has already removed many of the mis-defined haloes.

The value of $2T/U + 1$ for the TREE haloes is plotted against their mass in Fig. 5. We applied a QE cut of the form

$$-Q \leq \frac{2T}{U} + 1 \leq Q \quad (13)$$

to the TREE haloes, reducing Q gradually until the $\lambda(M_h)$

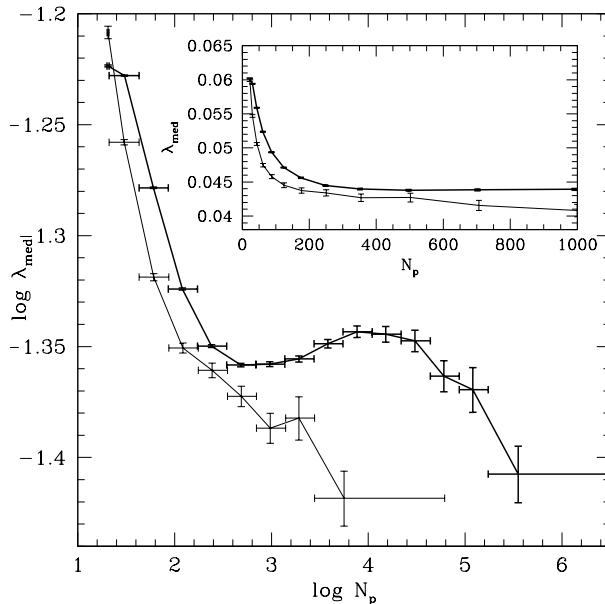


Figure 4. Median spins for all FOF haloes for the Millennium Run (thick line) and the **milli_lowres** run (thin line). The most massive bin contains 2000 haloes, and the remaining bins are logarithmically spaced, with one bin every factor of 2 in halo mass (except for the leftmost bin which extends down to the cutoff limit of 20 particles.) Horizontal bars mark the bin widths, and vertical error bars give a measure of the precision of the median according to Eqn. 12.

plot showed that the mis-defined haloes had been removed. This yielded a limit of $Q = 0.5$. These limits are shown on Fig. 5, and the resulting $\lambda(M_h)$ distribution is shown in Fig. 6. It is important to note that for an isolated object the spin should not depend on the state of virialisation. In reality however, these objects are never completely isolated, and the QE cut provides a useful tool with which to remove haloes with anomalous spins.

Having selected only QE haloes, we can now re-examine the effect of discreteness on the median spins. Fig. 7 shows $\lambda_{med}(N_p)$ for QE-selected FOF haloes, compared with QE-selected FOF haloes from **milli_lowres**. In contrast to Fig. 4, the two lines now lie on top of each other, exhibiting the same upturn in spin for haloes with the same number of particles. This demonstrates that the upturn is purely a numerical effect. We can exclude haloes that appear to be dominated by this effect by fixing a limit of $N_p \geq 300$ on the halo catalogue. Fig. 5 shows how the QE and N_p cuts relate to one another.

It is important to note that the criteria we have adopted are those appropriate to the quantities of interest in this work. For example, Fausti-Neto et al (in prep.) use the substructure parameter $S = \Delta r/R_{vir}$, where Δr is the distance between the potential minimum of the halo and its centre of mass. Their final criteria for selecting haloes in the Millennium simulation are $S < 0.07$ and $\frac{2T}{U} + 1 > -0.25$. They are concerned with fitting density profiles to haloes, and using the substructure parameter allows them to remove haloes with a large fraction of mass in substructures which would otherwise contaminate their results. Similarly, Macciò et al.

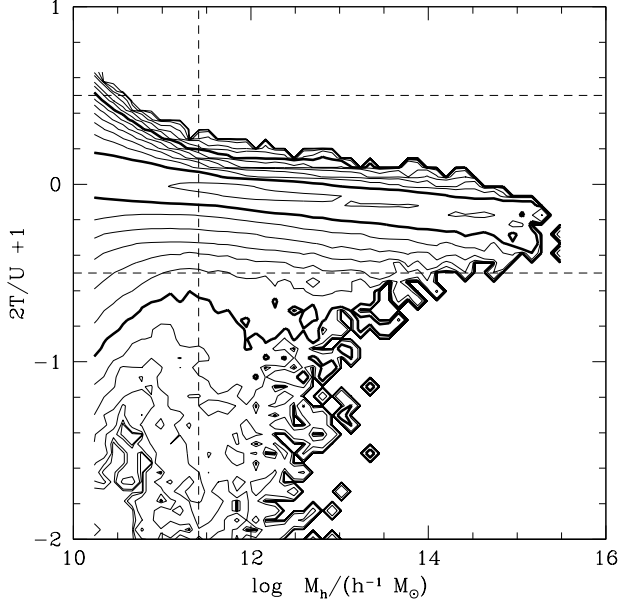


Figure 5. Contour plot of the instantaneous ‘virial ratio,’ $2T/U + 1$, against halo mass for TREE haloes. A virialised object has a value around zero. The tail at low values (large T) extends down to $2T/U + 1 \approx -960$; there are 3733 objects with $2T/U + 1 \leq -1$. The dashed lines show the QE limit of $Q = 0.5$, and the lower particle-number limit of $N_p = 300$. The contouring is as in Fig. 2, i.e. relative halo number density in equal logarithmic steps of size $10^{0.5}$. The inner bold contour represents 10^{-1} of the haloes at each mass, and the outer bold contour represents 10^{-4} of the haloes at each mass. The plots for FOF and SO groups are similar to this.

(2006) define an “offset parameter” as $x_{\text{off}} = \Delta r / R_{\text{vir}}$, where Δr is measured from the most-bound particle rather than the potential minimum. They use this alongside the rms of their density profile fits, to assess the quality of their halo catalogues for estimates of halo concentration. Although we have examined the substructure/offset parameter and how it affects λ , we find that it is not useful in removing the mis-defined haloes, or those whose spins are dominated by the numerical effects discussed above.

Having successfully cleaned our halo catalogues, we can now proceed to examine their spin properties.

4 RESULTS

4.1 The form of the spin distribution

The median spin of the TREE-QE- N_p halo catalogue is $\lambda_{\text{med}} = 0.0381$. The distribution of halo spins about the median, $P(\lambda)$, has been often fitted with a lognormal function (e.g. van den Bosch 1998; Gardner 2001; Bailin & Steinmetz 2005), i.e. a Gaussian in $\log \lambda$:

$$P(\log \lambda) = \frac{1}{\sigma_{\text{lg}} \sqrt{2\pi}} \exp \left[-\frac{\log^2 (\lambda/\lambda_0)}{2\sigma_{\text{lg}}^2} \right] \quad (14)$$

While this fitting function has proved adequate for small numbers of objects, we find that for the $> 10^6$ haloes in the Millennium simulation, deviations from a Gaussian are

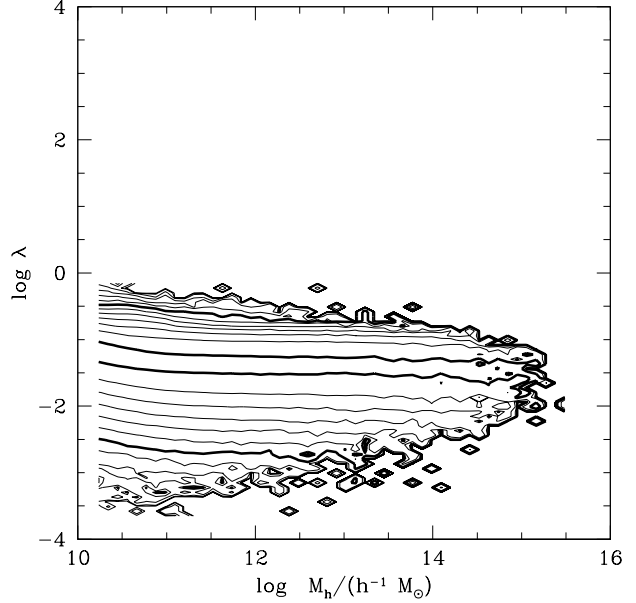


Figure 6. Spin parameter against halo mass for TREE haloes with a QE-limit of 0.5 applied; this can be compared with Figs 2 and 3. The same contouring is used, i.e. relative halo number density in equal logarithmic steps of size $10^{0.5}$. The inner bold contour represents 10^{-1} of the haloes at each mass, and the outer bold contour represents 10^{-4} of the haloes at each mass. The QE-limit has removed the vast majority of the high-spin haloes seen in Fig. 3.

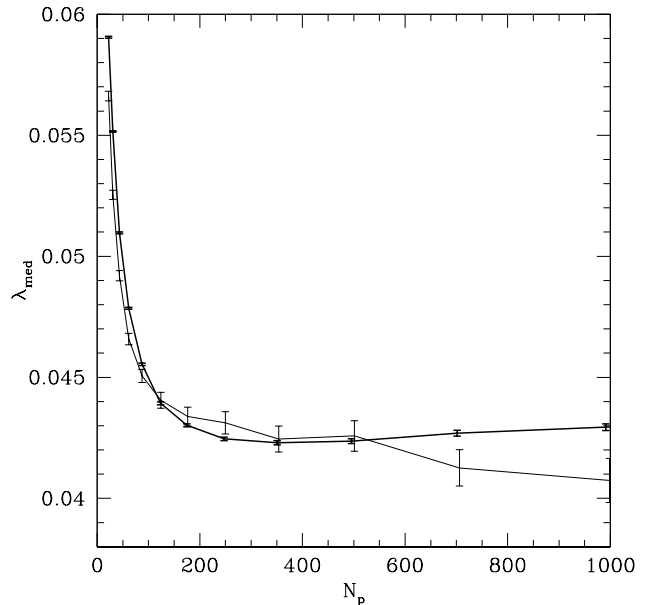


Figure 7. Median spins against number of particles in haloes, for FOF haloes with the QE cut applied. The thin line shows the `milli_lowres` haloes and the thick line shows those from the Millennium Run itself. The error bars show the uncertainty on the median, using Eqn. 12. The two lines show an identical trend at low N_p , demonstrating that the upturn in λ_{med} is indeed a numerical effect, affecting the spins of haloes containing fewer than about 300 particles.

clear and significant. The spin distribution drops faster than a Gaussian at high spins, and slower than a Gaussian at low spins. The best fit to the TREE-QE- N_p catalogue is shown in Fig. 8, which fits Eqn. 14 with peak location $\lambda_0 = 0.03687 \pm 0.000016$ and width $\sigma_{\text{lg}} = 0.2216 \pm 0.00012$.¹ The corresponding lognormal function of λ has the same peak, and a width of $\sigma = \ln(10)\sigma_{\text{lg}}$. This fit has a reduced- χ^2 of 40.46.

Part of the reason why a lognormal is such a poor fit is that this function strongly avoids very low spin values, whereas the real distribution does not. We have found that the following function provides a better description of the data:

$$P(\log \lambda) = A \left(\frac{\lambda}{\lambda_0} \right)^3 \exp \left[-\alpha \left(\frac{\lambda}{\lambda_0} \right)^{3/\alpha} \right] \quad (15)$$

For the normalised spin distribution, we can express A in terms of the other free parameters, α and λ_0 (the peak location):

$$A = 3 \ln 10 \frac{\alpha^{\alpha-1}}{\Gamma(\alpha)} \quad (16)$$

where the gamma function $\Gamma(\alpha) = (\alpha - 1)!$. The best fit to the data is shown in Fig. 9, and has parameters:

$$\lambda_0 = 0.04326 \pm 0.000020 \quad \alpha = 2.509 \pm 0.0033$$

with a much-improved reduced- χ^2 of 2.58.

We have also found the best fit of Eqn. 15 to the FOF-QE- N_p and SO-QE- N_p catalogues. The results for SO haloes are remarkably similar to those for the TREE haloes, with a reduced- χ^2 of 3.10:

$$\lambda_0 = 0.04174 \pm 0.000022 \quad \alpha = 2.540 \pm 0.0036$$

The median spin of the distribution is $\lambda_{\text{med}} = 0.0367$. The FOF haloes, which had a median spin $\lambda_{\text{med}} = 0.04288$, are not as well fitted by Eqn.15. The reduced- χ^2 is 15.0 and the parameter values are:

$$\lambda_0 = 0.04929 \pm 0.000027 \quad \alpha = 3.220 \pm 0.0046$$

This is, in fact, slightly worse than the best-fitting lognormal (Eqn. 14), which yields a reduced- χ^2 of 12.5, with a peak location $\lambda_0 = 0.04222 \pm 0.000022$ and width $\sigma_{\text{lg}} = 0.2611 \pm 0.00016$.

4.2 Correlation of spin and halo mass

The variation of median spin parameter with halo mass, for the three cleaned catalogues of TREE-QE, FOF-QE and SO-QE haloes, is shown in Fig. 10. It is interesting to note that the FOF haloes exhibit an upturn in spin for haloes more massive than the low- N_p cut, an effect that is not present in the TREE or SO haloes. This can be attributed to the outer parts of the FOF haloes consisting mainly of unbound ‘fuzz’ particles. These will, in general, have higher velocities, which act to inflate the spin until the surface particles form a negligible fraction of the halo mass. These particles are removed for the TREE haloes, and most will be shaved off in SO

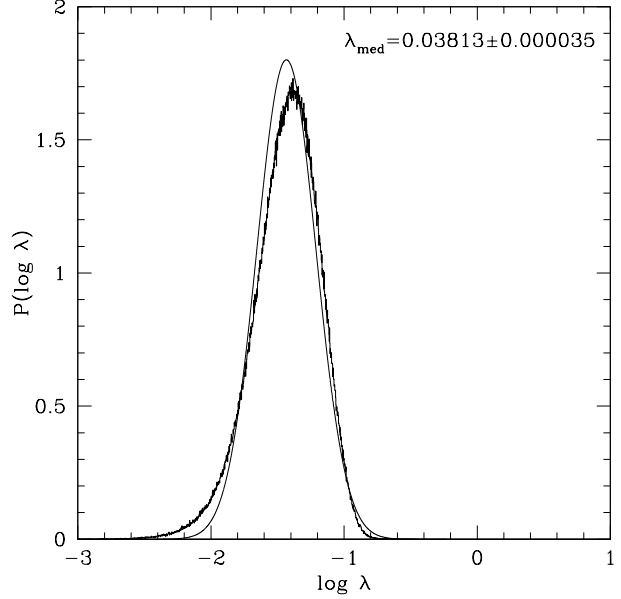


Figure 8. The normalised spin distribution (histogram) for merger-tree haloes with $N_p > 300$ and filtered using the QE criterion. The best-fitting single Gaussian function is plotted as the smooth curve. The Gaussian drops too quickly at low spins, and too slowly at higher spins. To try to minimize these effects, the best fit has a peak location that is shifted away from that of the histogram data. The median spin of the distribution is also displayed.

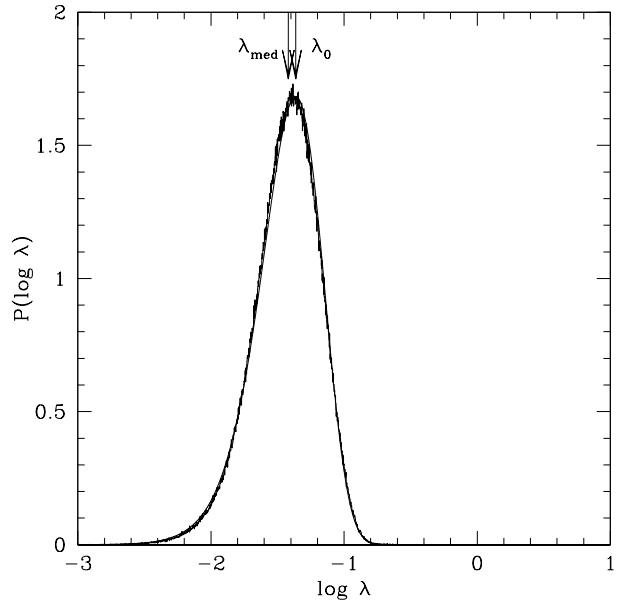


Figure 9. Histogram of the normalised $\log \lambda$ distribution of TREE-QE- N_p haloes, as in Fig. 8. The smooth solid curve is the best fit to the data using Eqn 15. The peak location of the fit (λ_0) and the median of the data (λ_{med}) are marked with arrows.

¹ Throughout this paper, the quoted uncertainties on best-fitting parameters are given by the square root of the diagonal of the covariance matrix for that fit.

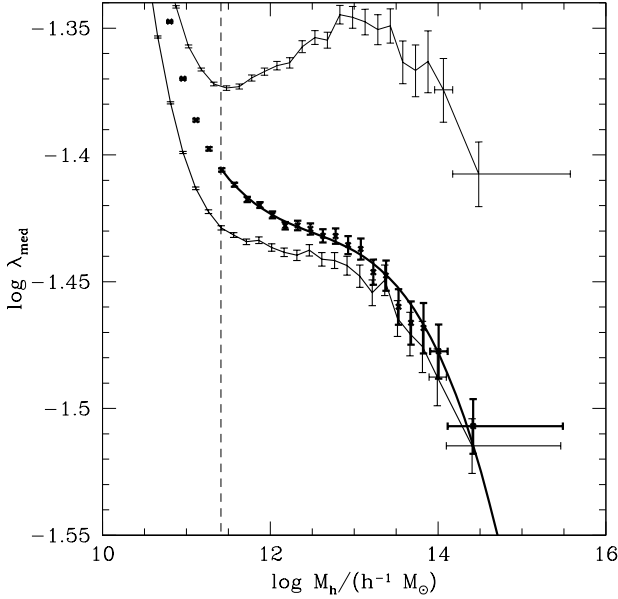


Figure 10. The median spins of halo mass bins, for TREE-QE haloes (bold points), SO-QE haloes (medium line) and FOF-QE haloes (thin line). The thick curve is the best-fitting cubic polynomial to the TREE-QE- N_p data. The vertical error bars are given by Eqn 12. The mass-binning scheme is similar to Fig. 4, but with bins every factor of $\sqrt{2}$ in mass. Only the widths of the most massive two bins are marked, for clarity. The low-mass limit ($M_h = 300m_p$) is marked with a dashed line.

haloes too. The SO and TREE haloes show a shallow downwards trend of λ_{med} up to $M_h \sim 10^{13} h^{-1} M_\odot \sim 12000 m_p$ and a rapid decline at larger masses.

We fit a cubic polynomial to the TREE-QE- N_p median spin data,

$$\log \lambda_{\text{med}} = \alpha x^3 + \beta x^2 + \gamma x + \delta \quad (17)$$

where $x = \log M_h / (h^{-1} M_\odot)$. The best-fitting values of these parameters are:

$$\begin{aligned} \alpha &= (-8.6 \pm 1.4) \times 10^{-3} \\ \beta &= (3.2 \pm 0.54) \times 10^{-1} \\ \gamma &= -4.1 \pm 0.68 \\ \delta &= 15.7 \pm 2.8 \end{aligned}$$

with a reduced- χ^2 of 0.44.

While the trend of λ_{med} with mass is real, it is important to note that it is a small effect; the scatter around this median is large (compare with Fig. 6, which shows data from the same haloes on a different $\log \lambda$ scale). This is in qualitative agreement with previous results (e.g. Cole & Lacey 1996), but because of its weak nature, this trend has often not been visible (e.g. Warren et al. 1992; Lemson & Kauffmann 1999; Macciò et al. 2006).

4.3 The halo shape distribution

The shapes of the haloes are described by the axes, $a \geq b \geq c$, of the ellipsoid derived from the inertia tensor, as described in Section 2.3. Fig. 11 shows the distributions of

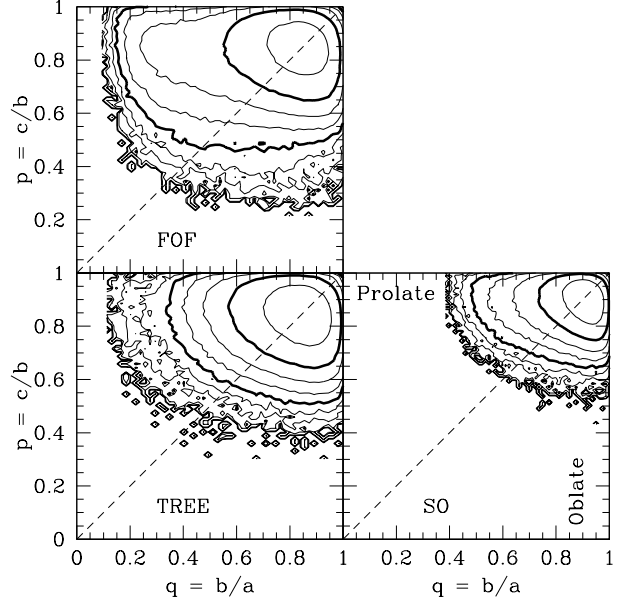


Figure 11. Axis ratios p and q for TREE, FOF and SO haloes (all with $Q = 0.5$ and $N_p \geq 300$). Prolate objects have $p = 1$, oblate objects have $q = 1$, and spherical objects have $p = q = 1$. The SO haloes are more spherical than the other two types. TREE and FOF objects exhibit a range of shapes, and all three catalogues show a preference for prolateness over oblateness. The contouring is by halo numbers, in equal logarithmic steps of $10^{0.5}$. In each plot, the inner bold contour represents 10^3 haloes, and the outer bold contour represents $10^{1.5}$ haloes.

$p = c/b$ and $q = b/a$ for the different halo catalogues. The haloes are generally triaxial, but they have a range of shapes, with a slight preference for prolateness over oblateness. The distribution agrees qualitatively with previous work such as that by Frenk et al. (1988), Warren et al. (1992), Cole & Lacey (1996), Faltenbacher et al. (2002) and Bailin & Steinmetz (2005). Unsurprisingly, SO haloes are more spherical than FOF or TREE haloes. FOF haloes show a much broader distribution of shapes (and a stronger preference for prolateness) than SO or TREE haloes.

Fig. 12 shows how the median shape of TREE-QE haloes changes with halo mass, using the minor-to-major axis ratio s and the triaxiality parameter $\mathcal{T} = (a^2 - b^2)/(a^2 - c^2)$. More massive haloes tend to be less spherical and more prolate. Again, this is in qualitative agreement with previous results, such as those of Warren et al. (1992), Bullock (2002), Kasun & Evrard (2005), Shaw et al. (2005), Gottlöber & Turchaninov (2006), Allgood et al. (2006), and Macciò et al. (2006). This is also what one might expect in a hierarchical formation model in which haloes tend to form by matter collapsing along filaments, leading to prolateness, rather than onto sheets which would lead to oblateness. Furthermore, the more massive haloes form later, and have had less time to relax into more spherical configurations. Since we have deliberately tried to select the more relaxed objects, the remaining trend we see here is weak. Furthermore, although the medians follow well-defined trends, the spread of the distribution in halo shapes covers virtually the entire

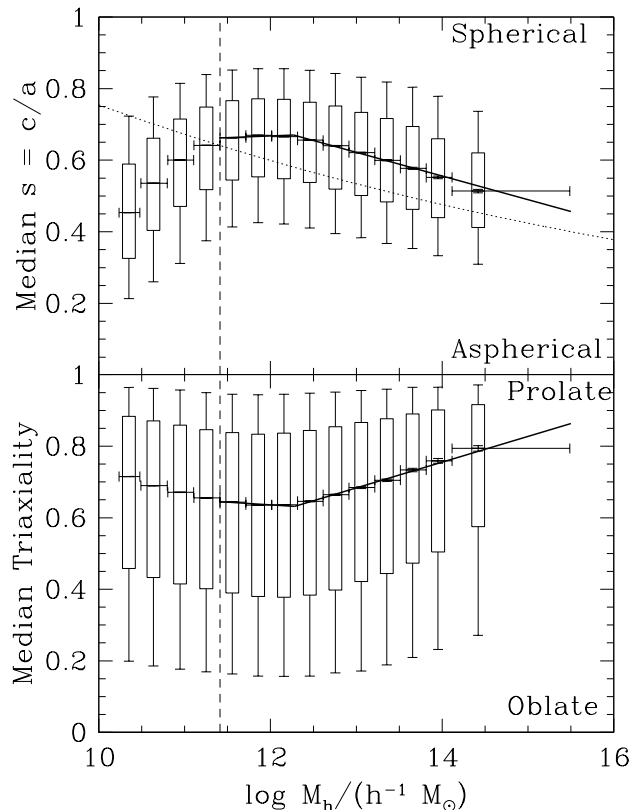


Figure 12. The median, in bins of halo mass, of the axis ratio s (top) and the triaxiality parameter \mathcal{T} (bottom), for TREE-QE haloes. The mass binning scheme is the same as in Fig. 4, and the low- N_p limit of 300 particles is marked with a dashed line. The medians for FOF-QE and SO-QE haloes follow the same behaviour as the TREE-QE haloes, but with SO haloes being more spherical and FOF less; FOF haloes are more prolate and SO haloes show a weaker preference for prolateness. Error bars on the medians (following Eqn. 12) are plotted, but most are vanishingly small. The whisker bars are percentiles, at the equivalent of 1σ (68% of haloes, boxes) and 2σ (95% of haloes, bars); from the bottom to the top of each graph, these show where approximately 2.5%, 16%, 84%, and 97.5% of the haloes have s (or \mathcal{T}) below these values. The thick lines show broken-line fits to the data; see the text for details. The dotted line is the fit of Allgood et al. 2006, who used a different definition of a halo (see text).

range in both s and \mathcal{T} , as can be seen from the percentile bars on the graph.

These two graphs both show a change in behaviour not seen in previous work, around the $N_p = 300$ limit. Resolution tests similar to those described in section 3.2 were carried out using the `milli_lowres` simulation, to assess whether this change in behaviour was indeed a numerical effect similar to that seen in halo spins (in Fig. 10). The results showed that these halo shape parameters do also require $N_p \gtrsim 300$, reinforcing our previous choice. Indeed, one would expect haloes whose spins are affected by particle discreteness (i.e. with $N_p \lesssim 300$) to be less spherical and more stringy (prolate).

We fit a broken line to both shape parameters, of the form:

$$y_{\text{med}}(x) = \begin{cases} m_1 x + c_1 & x \leq x_0 \\ m_2 x + c_2 & x \geq x_0 \end{cases} \quad (18)$$

where $x = \log M_h / (h^{-1} M_\odot)$. We fit with m_1 , m_2 , x_0 and c_2 as free parameters, with $c_1 \equiv c_2 + (m_2 - m_1)x_0$. The fitted parameters for s_{med} are:

$$\begin{aligned} m_{1,s} &= (9.2 \pm 0.87) \times 10^{-3}, & c_{1,s} &= 0.56 \pm 0.015, \\ m_{2,s} &= (-6.6 \pm 0.12) \times 10^{-2}, & c_{2,s} &= 1.48 \pm 0.015, \\ x_{0,s} &= 12.27 \pm 0.012 \end{aligned}$$

with a reduced- χ^2 of 29.9. The fitted parameters for \mathcal{T}_{med} are:

$$\begin{aligned} m_{1,\mathcal{T}} &= (-1.6 \pm 0.18) \times 10^{-2}, & c_{1,\mathcal{T}} &= 0.82 \pm 0.031, \\ m_{2,\mathcal{T}} &= (7.2 \pm 0.24) \times 10^{-2}, & c_{2,\mathcal{T}} &= -0.25 \pm 0.029, \\ x_{0,\mathcal{T}} &= 12.28 \pm 0.021 \end{aligned}$$

with a reduced- χ^2 of 4.27. The two mass breakpoints $x_{0,s}$ and $x_{0,\mathcal{T}}$ agree within their uncertainties.

Allgood et al. (2006) fit a power-law to $s_{\text{med}}(M_h)$. This is plotted in Fig. 12, and indicates that their haloes are significantly less spherical than ours. This is largely a result of different group definitions; although not plotted, we find that our SO-QE and FOF-QE catalogues differ from the TREE-QE results by a similar amount. A power-law of the type used by Allgood et al. (2006) would not be a good fit to the data presented here which have a definite change in slope towards lower halo masses.

4.4 Spin and shape parameters

The relationship between spin parameter and halo shape is illustrated in Figs 13, 14 and 15. Fig. 14 emphasizes the trend visible in Fig. 13 by plotting the median spin parameter as a function of s for different mass bins. There is a clear trend for more spherical haloes to exhibit less coherent rotation. Although this trend is in the sense one might naïvely expect, the haloes, in fact, do not have very high spin, and are not rotationally supported. The origin of this trend is likely to lie instead in the effects of the tidal torques experienced by the haloes during their early phases of formation.

As seen previously in Fig. 10, the least massive objects have the most extreme spins, in the median. Fig. 14 shows that the higher spin objects are also the less spherical. The haloes which are closest to spherical have a spin parameter that is independent of halo mass, and has $\lambda_{\text{med}} \approx 0.033$. (This does not apply to the most massive haloes, however, since their population lacks the more spherical objects). Furthermore, the median spins for the more massive haloes are independent of shape and have $\lambda_{\text{med}} \approx 0.032$.

In contrast to the variation λ_{med} with s , Fig. 15 shows that there is only a very weak trend of spin with halo triaxiality. Over the entire range of triaxiality, each \mathcal{T} -bin contains a very similar fraction of haloes at each value of $\log \lambda$.

4.5 Spin-shape alignment

Fig. 16 shows the angle between the angular momentum vector and the three shape axis vectors, e.g.:

$$\cos \theta_a = |\mathbf{j} \cdot \hat{\mathbf{a}} / j| \quad (19)$$

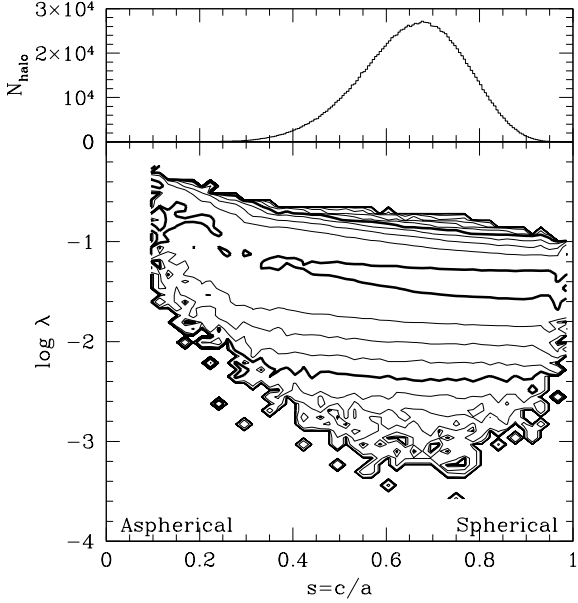


Figure 13. The main plot shows spin versus axis ratio $s = c/a$ for TREE-QE- N_p haloes; contouring is similar to Fig. 2, showing the number density of haloes, normalised by the number of haloes in each s -bin. The inner bold contour represents 10^{-1} of the haloes in each s -bin, the outer bold contour represents 10^{-3} of the haloes in each s -bin, and the contours are spaced in equal logarithmic steps of $10^{0.5}$. The upper plot is a histogram of s for TREE-QE- N_p haloes, effectively showing the function by which the contour plot has been normalised.

for alignment with the semimajor axis given by the unit vector \hat{a} . Note that this definition does not distinguish between \mathbf{j} lying parallel or antiparallel to the axis vectors.

Most haloes have their spin axis well aligned with their minor axis, and lying perpendicular to their major axis. However, the distribution of alignments with respect to all three axes is fairly broad. This agrees with previous results (e.g. Warren et al. 1992, Bailin & Steinmetz 2005, Allgood et al. 2006 and Shaw et al. 2005).

Extremely oblate objects have a degeneracy between the major and intermediate axes ($\frac{b}{a} \sim 1$), so there is an equal probability for the angular momentum vector to subtend a given angle with either axis. This can be seen in the top-left panel of Fig. 17 which shows the alignment distribution for the more oblate haloes, i.e. those with $\mathcal{T} < 0.2$ (and $s < 0.8$ in order to avoid an $a \sim b \sim c$ degeneracy). Since most haloes have \mathbf{j} aligned with \hat{c} , \mathbf{j} has a preference for being at right angles to the two large axes.

For extremely prolate haloes, the degeneracy is between minor and intermediate axes ($\frac{c}{b} \sim 1$). In this case, the distribution of the alignment of the angular momentum vector with either of these axes is similar only for the tail of extremely prolate haloes, $\mathcal{T} > 0.99$ (bottom-right panel). For $\mathcal{T} > 0.8$, only a small number of haloes have their spin axis aligned with the intermediate axis (top-right panel); like the bulk of the population as a whole, most of these haloes rotate around their smallest axis.

The reason for the distinction between the major and intermediate axes present in Fig. 16 can now be seen to be

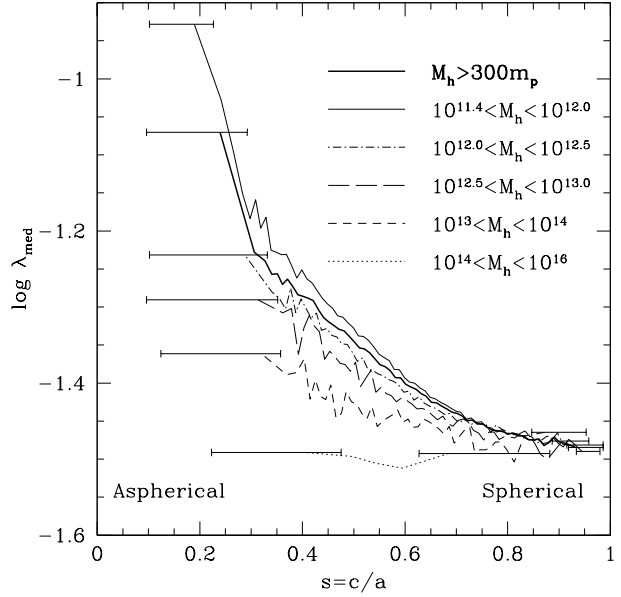


Figure 14. The median spin parameter in bins of axis ratio $s = c/a$, for TREE-QE haloes. The heavy line is for all haloes with more than 300 particles (the full TREE-QE- N_p catalogue); the other lines show the trends for different halo mass bins. The horizontal bars show the widths of the first and last bins for each line. The trend is for more spherical haloes to have less coherent rotation in the median. This trend becomes very steep for the most aspherical haloes (although these are not present at higher masses because of the rapid drop in the halo mass function).

a combination of various effects. The preference for prolateness over oblateness means that there is a tendency for the intermediate axis to be more similar to the minor than to the major axis. This increases the probability of \mathbf{j} being aligned to the \hat{b} axis. However, since \mathbf{j} can be aligned with only one axis (and when this happens it must be perpendicular to the other two), the preference for the spin axis to be the minor axis outweighs the preference for prolateness, and this results in the slight excess probability for \mathbf{j} to be perpendicular to the intermediate axis seen in the figure.

4.6 Two-point correlation functions

In this section, we investigate whether there is an environmental dependence of halo spin. We quantify environment by means of the two-point correlation function, $\xi(r)$, of the haloes, and we explore whether the clustering amplitude differs for haloes with different spin. The three halo catalogues were divided into four bins in halo mass, and the haloes in each mass bin were then divided about the median spin for that mass; $\xi(r)$ was calculated for each set of haloes. The results are plotted in Figs 18 and 19 for the TREE-QE- N_p and FOF-QE- N_p catalogues respectively. (The results for SO-QE- N_p haloes are very similar to the FOF results.) The lines in Fig. 18 show power-law fits over the limited range of pair separations shown,

$$\xi(r) = \left(\frac{r}{r_0}\right)^\gamma. \quad (20)$$

The fitted values of r_0 and γ are given in Table 3.

Mass bin ($h^{-1}M_{\odot}$)	$\lambda < \lambda_{\text{med}}$		$\lambda \geq \lambda_{\text{med}}$	
	γ	$r_0/(h^{-1}\text{Mpc})$	γ	$r_0/(h^{-1}\text{Mpc})$
$10^{11.4}-10^{12}$	-1.553 ± 0.0013	3.670 ± 0.0070	-1.489 ± 0.0012	3.671 ± 0.0073
$10^{12}-10^{13}$	-1.591 ± 0.0031	4.22 ± 0.020	-1.537 ± 0.0026	4.82 ± 0.021
$10^{13}-10^{14}$	-1.64 ± 0.021	6.6 ± 0.24	-1.71 ± 0.016	8.3 ± 0.23
$10^{14}-10^{16}$	-1.6 ± 0.19	13 ± 5.8	-1.7 ± 0.12	19 ± 4.8

Table 3. Parameters for the power-law $\xi(r) = (r/r_0)^\gamma$ from fitting to the eight two-point correlation functions for TREE-QE- N_p haloes.

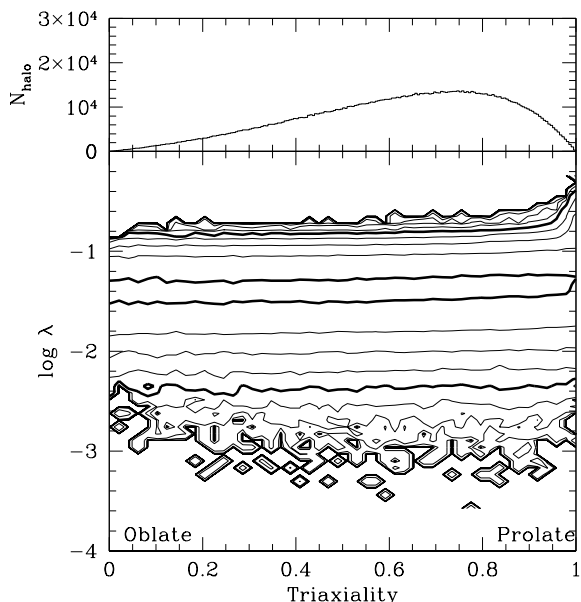


Figure 15. The main plot shows spin versus triaxiality parameter T for TREE-QE- N_p haloes; contouring is as for Fig. 13, i.e. in equal logarithmic steps of $10^{0.5}$ haloes per T -bin. The inner bold contour represents 10^{-1} of the haloes in each T -bin, and the outer bold contour represents 10^{-3} of the haloes in each T -bin. The upper plot is a histogram of T for TREE-QE- N_p haloes, effectively showing the function by which the contour plot has been normalised.

For the higher mass bins, the results from the different types of haloes are similar: higher spin haloes are more strongly clustered than lower spin haloes. This could be because objects evolving in denser, more clustered environments are more likely to experience stronger tidal forces, leading to more coherent rotation. These results are consistent with the tentative earlier work of Barnes & Efstathiou (1987), as well as the mark correlation function analysis of Faltenbacher et al. (2002)

The difference in clustering strength between high and low spin haloes decreases with halo mass. For the least massive TREE haloes, $M = 10^{11.4}-10^{12} h^{-1}M_{\odot}$, there is virtually no difference in the correlation functions of the fast and slow rotators.

Note that the ‘cleaner’ sample, i.e. the TREE haloes exhibits stronger clustering in general, for all but the highest masses. This is due to the fact that the splitting algorithm applied during the construction of the merger trees results

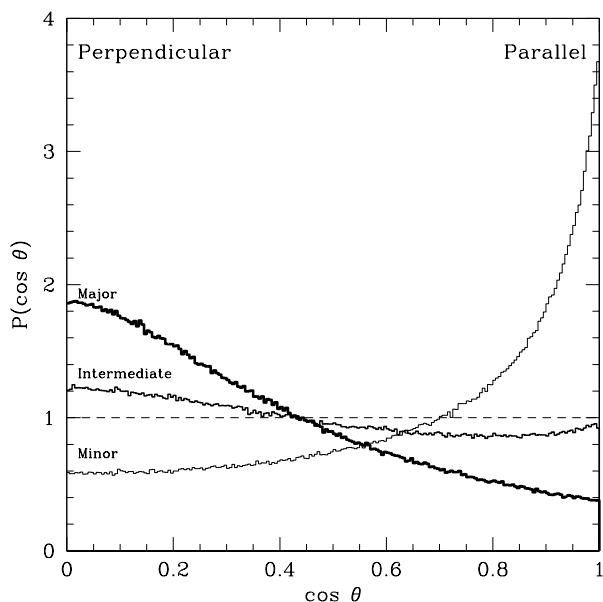


Figure 16. Normalised histograms of the cosines of the angle between the angular momentum vector and the major (thick line), intermediate (medium line) and minor (thin line) axes of TREE-QE- N_p haloes, as defined in the text. A random distribution would be a flat line at $P(\cos \theta) = 1$.

in a greater number of close halo neighbours (albeit with reduced masses) compared to the corresponding FOF haloes.

We have performed a similar analysis to that presented in Figs. 18 and 19 for the halo sphericity parameter, s . We found analogous results, in that the more spherical haloes are more clustered than the less spherical haloes. To examine the effect of halo spin and shape on clustering in more detail, we consider the bias parameter, b , which describes how much more or less clustered a set of haloes is relative to the underlying dark matter distribution. We examine how the bias varies for haloes with different values of λ or s , at a fixed range of mass. Similar analyses have recently been performed by Gao et al. (2005), Wechsler et al. (2005) and Wetzell et al. (2006), who examined the effect of halo formation time, concentration, substructure content and time since last major merger on the bias. The bias parameter is related to the correlation function through:

$$\xi_{hh}(r|M_h, \lambda) = b^2(r|M_h, \lambda)\xi_{mm}(r) \quad (21)$$

where $\xi_{hh}(r|M_h, \lambda)$ denotes the halo-halo correlation function for haloes in a given range of mass and spin (in this

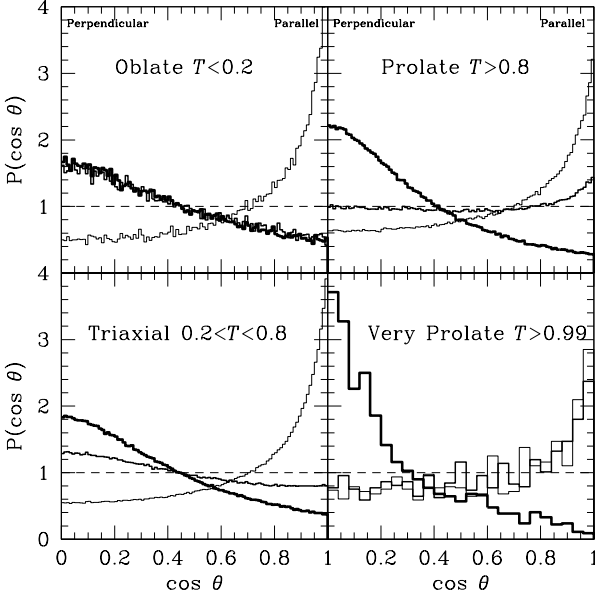


Figure 17. Normalised histograms of the cosine of the angle between the specific angular momentum vector and the major (thick line), intermediate (medium line) and minor (thin line) axes of the haloes. The TREE-QE- N_p haloes have been cut at the values of the triaxiality parameter shown. The most spherical haloes ($s > 0.8$) have been removed from each sample. The ‘very prolate’ selection only contains 1360 groups, giving rise to a noisier histogram.

example), and $\xi_{mm}(r)$ is the dark matter correlation function.

We compute the bias parameter as a function of mass, $b(M_h)$, using a similar method to that of Gao et al. (2005). Specifically, we compute $\xi_{hh}(r|M_h, \lambda)$ in four r -bins in the range $6 \leq r \leq 25 h^{-1} \text{Mpc}$, equally spaced in $\log r$. The bias parameter at each mass is then found as the normalisation constant that minimises:

$$\chi^2 = \sum_{i=1}^4 \left(\frac{\xi_{hh}(r_i) - b^2 \xi_{mm}(r_i)}{\sigma_{hh}(r_i)} \right)^2 \quad (22)$$

where the $\sigma_{hh}(r_i)$ are the Poisson errors on $\xi_{hh}(r_i)$. This procedure is performed first for all the TREE-QE- N_p and FOF-QE- N_p haloes. It is then repeated for the haloes in the upper and lower 20th percentiles of the λ and s distributions, from both catalogues.

The results are shown in figure 20. This shows that higher spin haloes are more clustered than the average, and the lower spin haloes are less clustered. This trend is largest at higher masses, reaching a factor of ≈ 2.7 between the high-spin and low-spin bias at the largest mass, $\sim 10^{14} h^{-1} \text{M}_\odot$.

5 CONCLUSIONS

The huge size and high resolution of the Millennium simulation (Springel et al. 2005) makes it possible to determine the properties of dark matter haloes in the ΛCDM cosmology with unprecedented statistical power. In this paper, we

have concentrated on the spins and shapes of dark matter haloes, ranging in mass from those of dwarf galaxies to those of rich clusters. We have investigated the distribution of the spin parameter, λ , its dependence on mass, the distribution of shapes, the relationship between shape and spin and the environmental dependence of spin. We provide accurate fitting formulae for several quantities of interest.

While many of the properties we have investigated here have been studied in earlier simulations going back over twenty years, a novel aspect of our work is the analysis and comparison of haloes identified in different ways. Alongside the traditional ‘friends-of-friends’ (FOF) algorithm of Davis et al. (1985) and the ‘spherical overdensities’ (SO) algorithm of Cole and Lacey (1994), we have introduced a new definition of a halo, the TREE haloes, which are perhaps the most appropriate when carrying out comparisons of the simulation results with galaxy and cluster data. The TREE haloes are defined as branches of the halo merger trees in which special care has been taken to identify physical haloes by separating objects that are artificially and transiently linked together. Our catalogues consist of $> 10^6$ haloes at $z = 0$.

The TREE halo catalogue was further ‘cleaned’ in two ways. Firstly, to remove any remaining spurious objects, we applied a cut in the instantaneous virial ratio, $(-0.5 \leq \frac{2T}{U} + 1 \leq 0.5)$. Secondly, to remove objects whose angular momentum is biased due to particle discreteness, we considered only haloes with more than 300 particles, as indicated by convergence tests.

We find that the distribution of the dimensionless spin parameter, $P(\log \lambda)$, is poorly fit by a lognormal when this many objects are considered. The function given by Eqn. 15 provides a much better description of the data. Although the distribution of $\lambda(M_h)$ is fairly broad, there is a clear trend of the median spin with halo mass, with more massive haloes spinning more slowly. However, the strength and shape of the trend is significantly different for different halo definitions. The cubic polynomial of Eqn. 17 provides a very good fit to the median spin of TREE haloes, over a factor of $\sim 10^3$ in halo mass.

We analysed the shapes of the haloes, and found, as in previous studies, that there is a broad distribution of shapes with a slight preference for prolateness over oblateness. More massive haloes are less spherical and more prolate in the median, although the data span a large fraction of the available shape parameter space. We fit broken lines to the trends with $\log M_h$ of the median sphericity axis ratio $s = c/a$ and the median triaxiality parameter \mathcal{T} (Eqn. 18). Both these quantities exhibit a change of behaviour at a galactic mass scale, $M_h \approx 2 \times 10^{12} h^{-1} \text{M}_\odot$ where the gradient of the fit changes sign, haloes becoming increasingly aspherical and more prolate with increasing mass.

The rounder haloes have less coherent rotation, with a median spin that is independent of mass ($\lambda_{\text{med}}(s \gtrsim 0.9) \approx 0.033$). The most massive haloes have a median spin that is independent of sphericity ($\lambda_{\text{med}}(s) \approx 0.032$). However, there is significantly less correlation between the nature of halo triaxiality (prolateness *vs* oblateness) and spin parameter. Although the haloes are far from being rotationally supported, there is a strong preference for the spin vector to be aligned parallel to the halo minor axis and to be perpendicular to the major axis. The tendency for the spin to be

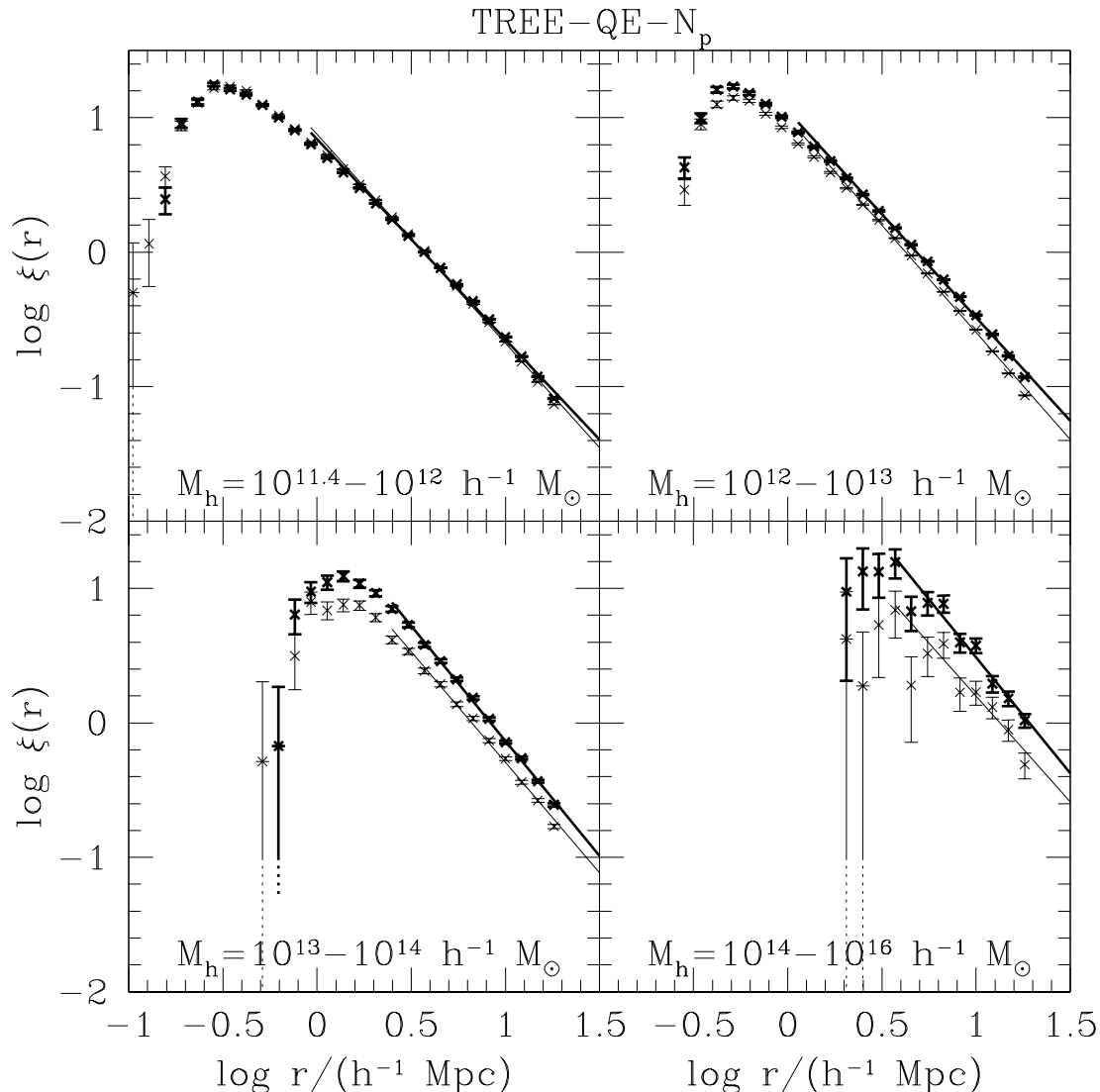


Figure 18. Two-point correlation function, $\xi(r)$, for TREE-QE- N_p haloes in four mass bins. The lines represent power-law fits over the r -bins shown. The thick lines and points are for haloes with $\lambda \geq \lambda_{\text{med}}$ for that mass bin; the thin lines and points are for haloes with $\lambda < \lambda_{\text{med}}$. The data are noisy in the higher mass bins which contain fewer haloes. The error bars are Poisson errors, i.e. the square-root of the number of pairs in each r -bin, divided by the mean number of pairs per r -bin.

perpendicular to the intermediate axis is significantly weakened by the prevalence of prolate shapes for which there is a near degeneracy between the intermediate and minor axes.

We find a clear signal that the spins and shapes of haloes are sensitive to the cosmological environment: more rapidly rotating haloes of a given mass are more strongly clustered. The strength of this effect increases with halo mass. It is weak for subgalactic and galactic haloes, but can be larger than a factor of ~ 2 for galaxy cluster haloes. A similar effect is seen when examining halo shapes: more spherical haloes are more strongly clustered, with a greater signal at higher masses. Our result adds further evidence to the recent finding by Gao et al. (2005), also from analysis of the Millennium Run, that the internal properties of haloes depend not only upon their mass but also upon the environment in which they form.

The huge number of haloes in the Λ CDM Millennium

simulation enables us to characterise the distribution of halo spins, and their relation to halo mass, shape and clustering, with unprecedented precision. However, we have also shown the significance of a careful halo definition. The properties of haloes defined and identified in different ways are noticeably different, and it is important to make the appropriate choice for a given application. For comparisons with real data, we recommend using the new class of “TREE” haloes which we have investigated in this work.

ACKNOWLEDGEMENTS

PB acknowledges receipt of a PhD studentship from the Particle Physics and Astronomy Research Council. VRE is a Royal Society University Research Fellow. CSF is a Royal Society-Wolfson Research Merit Award holder. The simu-

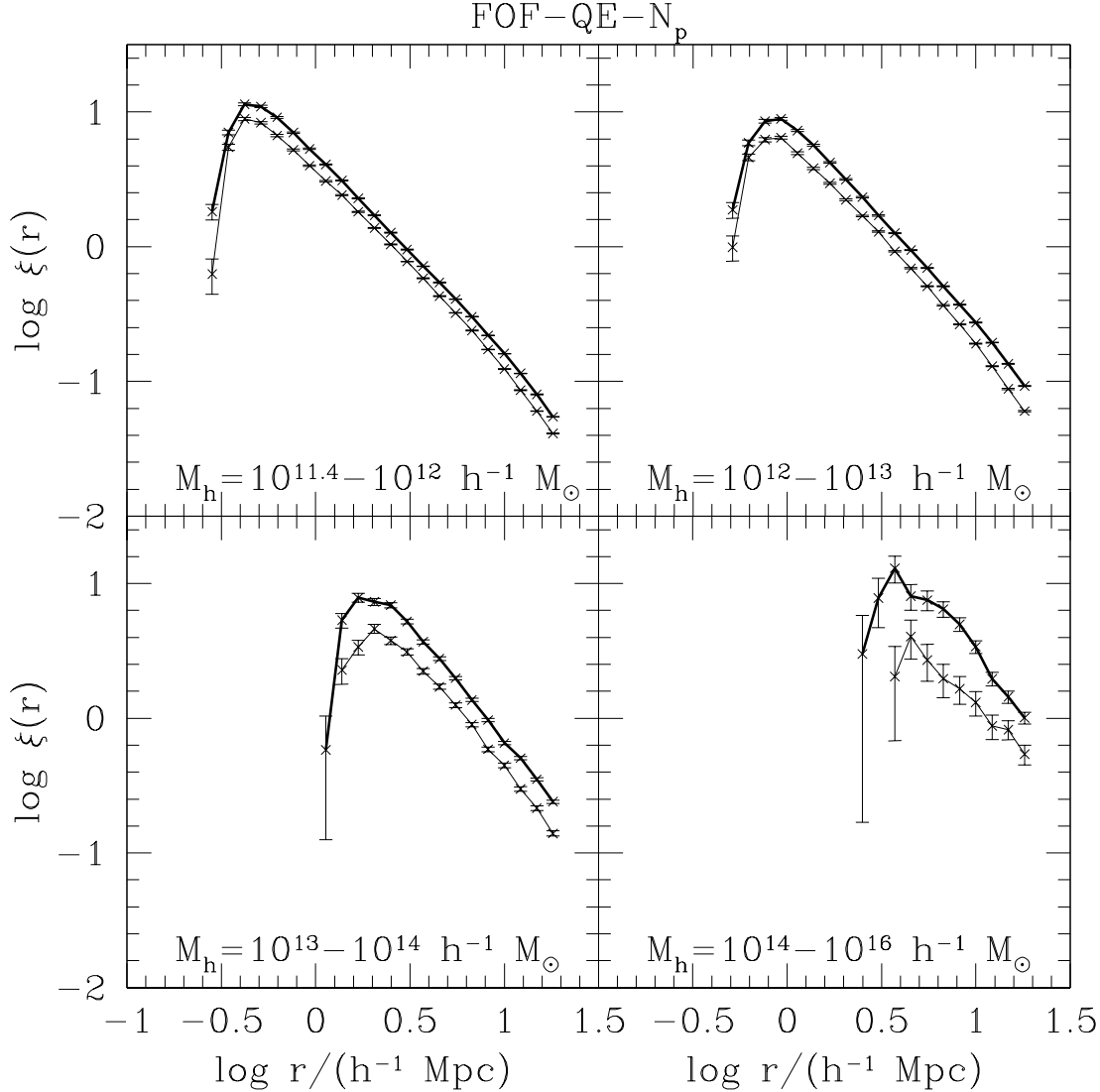


Figure 19. As Fig. 18, but for the FOF-QE- N_p haloes. No fits were made to these data, and the lines merely join the points. For this catalogue, the higher spin haloes (thick lines) are consistently and significantly more strongly clustered than the lower spin haloes (thin lines). The results for the SO-QE- N_p haloes are very similar.

lation and analysis used in this paper was carried out as part of the programme of the Virgo Consortium on the Regatta supercomputer of the Computing Centre of the Max-Planck-Society in Garching, and the Cosmology Machine supercomputer at the Institute for Computational Cosmology, Durham.

REFERENCES

- Allgood B., Flores R. A., Primack J. R., Kravtsov A. V., Wechsler R. H., Faltenbacher A., Bullock J. S., 2006, *MNRAS*, 367, 1781
- Avila-Reese V., Colín P., Gottlöber S., Firmani C., Mautsch C., 2005, *ApJ*, 634, 51
- Bailin J., Steinmetz M., 2005, *ApJ*, 627, 647
- Barnes J., Efstathiou G., 1987, *ApJ*, 319, 575
- Bower R. G., Benson A. J., Malbon R., Helly J. C., Frenk C. S., Baugh C. M., Cole S., Lacey C. G., 2005, preprint (astro-ph/0511338)
- Bryan G. L., Norman M. L., 1998, *ApJ*, 495, 80
- Bullock J. S., 2002, in Natarajan P., ed., *Proceedings of the Yale Cosmology Workshop “The Shapes of Galaxies and Their Dark Matter Halos”*, New Haven, Connecticut, USA, 28-30 May 2001. Singapore: World Scientific, 2002, ISBN 9810248482. Shapes of dark matter halos (astro-ph/0106380). p. 109
- Catelan P., Theuns T., 1996, *MNRAS*, 282, 436
- Cole S., Lacey C., 1996, *MNRAS*, 281, 716
- Cole S., Lacey C. G., Baugh C. M., Frenk C. S., 2000, *MNRAS*, 319, 168
- Davis M., Efstathiou G., Frenk C. S., White S. D. M., 1985, *ApJ*, 292, 371
- Doroshkevich A. G., 1970, *Astrophysics*, 6, 320
- Efstathiou G., Jones B. J. T., 1979, *MNRAS*, 186, 133

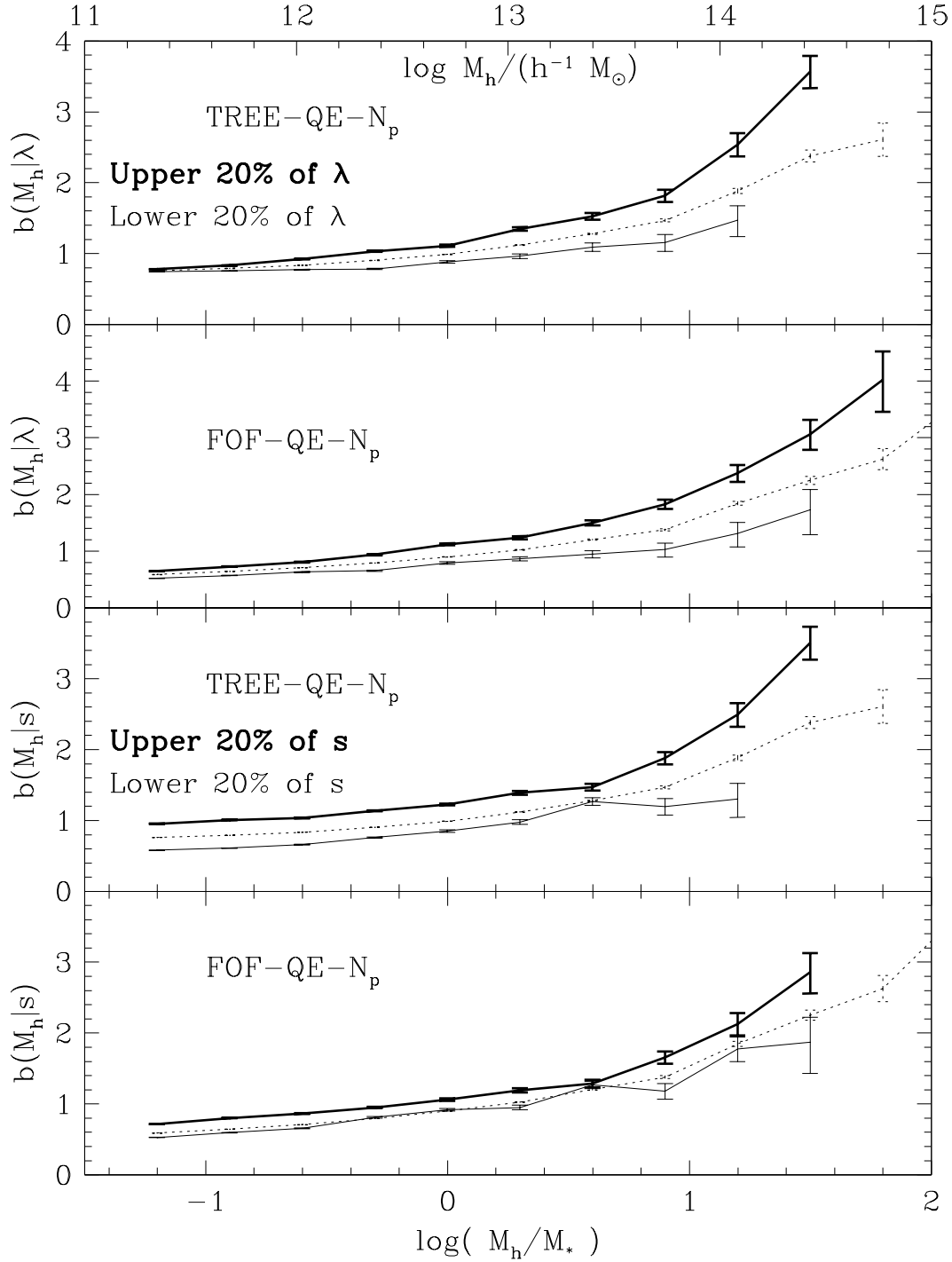


Figure 20. Bias parameter, $b(M_h)$, for the halo populations indicated in the legend. In each plot, the central dotted line marks the bias for the entire population at that mass. The thick line is the bias for haloes in the upper 20 per cent of the distributions of λ (upper two plots) and s (lower two plots), and the thin line is for haloes in the lower 20 per cent of the distributions. The error bars give the $\Delta\chi^2 = 1$ confidence interval.

Eke V. R., Cole S., Frenk C. S., 1996, MNRAS, 282, 263
 Faltenbacher A., Gottlöber S., Kerscher M., Müller V., 2002, A&A, 395, 1
 Franx M., Illingworth G., de Zeeuw T., 1991, ApJ, 383, 112
 Frenk C. S., White S. D. M., Davis M., Efstathiou G., 1988, ApJ, 327, 507
 Gao L., Springel V., White S. D. M., 2005, MNRAS, 363, L66
 Gardner J. P., 2001, ApJ, 557, 616
 Gottlöber S., Turchaninov V., 2006, in EAS Publications Series. Halo Shape and its Relation to Environment (astro-ph/0511675). pp 25–28
 Harker G., Cole S., Helly J., Frenk C., Jenkins A., 2005, preprint (astro-ph/0510488)
 Helly J. C., Cole S., Frenk C. S., Baugh C. M., Benson A., Lacey C., 2003, MNRAS, 338, 903
 Hopkins P. F., Bahcall N. A., Bode P., 2005, ApJ, 618, 1
 Hoyle F., 1949, in Burgers J. M., van de Hulst H. C., eds, Problems of Cosmical Aerodynamics, The origin of the rotations of the galaxies. Central Air Documents Office, Dayton, OH, pp 195–197
 Kasun S. F., Evrard A. E., 2005, ApJ, 629, 781
 Lacey C., Cole S., 1994, MNRAS, 271, 676
 Lee J., Pen U.-L., 2000, ApJ, 532, L5
 Lemson G., Kauffmann G., 1999, MNRAS, 302, 111
 Macciò A. V., Dutton A. A., van den Bosch F. C., Moore B., Potter D., Stadel J., 2006, preprint (astro-ph/0608157)
 Mo H. J., Mao S., White S. D. M., 1998, MNRAS, 295, 319
 Padmanabhan T., 1993, Structure formation in the Universe. Cambridge Univ. Press, Cambridge
 Peebles P. J. E., 1969, ApJ, 155, 393
 Peebles P. J. E., 1971, A&A, 11, 377
 Percival W. J., et al., 2002, MNRAS, 337, 1068
 Porciani C., Dekel A., Hoffman Y., 2002, MNRAS, 332, 325
 Reed D., Governato F., Quinn T., Gardner J., Stadel J., Lake G., 2005, MNRAS, 359, 1537
 Sánchez A. G., Baugh C. M., Percival W. J., Peacock J. A., Padilla N. D., Cole S., Frenk C. S., Norberg P., 2006, MNRAS, 366, 189
 Shaw L., Weller J., Ostriker J. P., Bode P., 2005, preprint (astro-ph/0509856)
 Spergel D. N., et al., 2003, ApJS, 148, 175
 Spergel D. N., et al., 2006, preprint (astro-ph/0603449)
 Springel V., et al., 2005, Nature, 435, 629
 Springel V., White S. D. M., Tormen G., Kauffmann G., 2001, MNRAS, 328, 726
 Springel V., Yoshida N., White S. D. M., 2001, New Astronomy, 6, 79
 Tegmark M., et al., 2004, Phys. Rev. D, 69, 103501
 Tonini C., Lapi A., Shankar F., Salucci P., 2006, ApJ, 638, L13
 van den Bosch F. C., 1998, ApJ, 507, 601
 Warren M. S., Quinn P. J., Salmon J. K., Zurek W. H., 1992, ApJ, 399, 405
 Wechsler R. H., Zentner A. R., Bullock J. S., Kravtsov A. V., Allgood B., 2005, preprint (astro-ph/0512416)
 Wetzel A. R., Cohn J. D., White M., Holz D. E., Warren M. S., 2006, preprint (astro-ph/0606699)
 White S. D. M., 1984, ApJ, 286, 38
 White S. D. M., Frenk C. S., 1991, ApJ, 379, 52
 White S. D. M., Rees M. J., 1978, MNRAS, 183, 341

APPENDIX A: EXAMPLES OF HALOES

The following plots show examples of haloes from our catalogues. Figs A1, A2 and A3 show FOF haloes with unusual properties, illustrating some of the cuts made to the catalogues. We show a halo that is clearly made up of at least two objects joined via tenuous bridge in Fig. A1. Fig. A2 shows a more massive halo that nevertheless consists of many linked objects. Fig. A3 shows a very distorted object located near a much larger halo. Each Fig. shows projections in real space and velocity space.

Figs A4 and A5 compare haloes defined using the FOF, SO and TREE algorithms. In both cases, projections of the selected FOF halo (and its neighbours) are shown in the left-hand panels, and the corresponding SO/TREE halo and neighbours are in the right-hand panels.

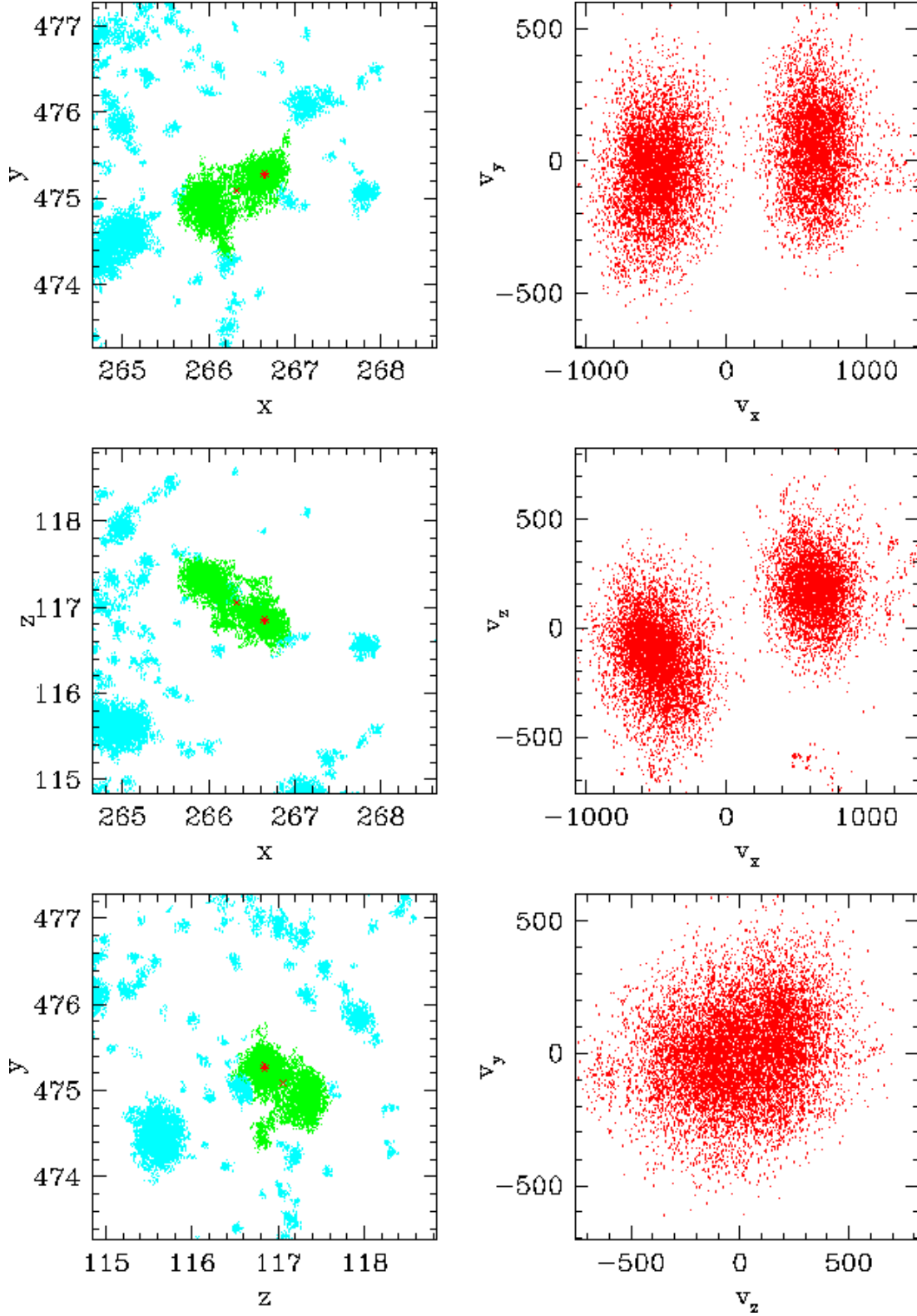


Figure A1. An example of a FOF halo made of two objects linked by a tenuous bridge. The left-hand panels show projections of the halo (overplotted in green) and its neighbours within $2 h^{-1}\text{Mpc}$ (blue) in real space, in units of $h^{-1}\text{Mpc}$. The potential-minimum centre of the main halo is marked with a red star, and the centre-of-mass is marked with a red cross. The right-hand panels show the particles of the selected halo in velocity space, in km s^{-1} . This halo has a mass of $M_h = 11418 m_p \approx 9.82 \times 10^{12} h^{-1} M_\odot$, and a spin parameter of $\lambda = 1.5712$. Its virial ratio, $\frac{2T}{U} + 1 = -4.23$ means it is excluded from the FOF-QE catalogue.

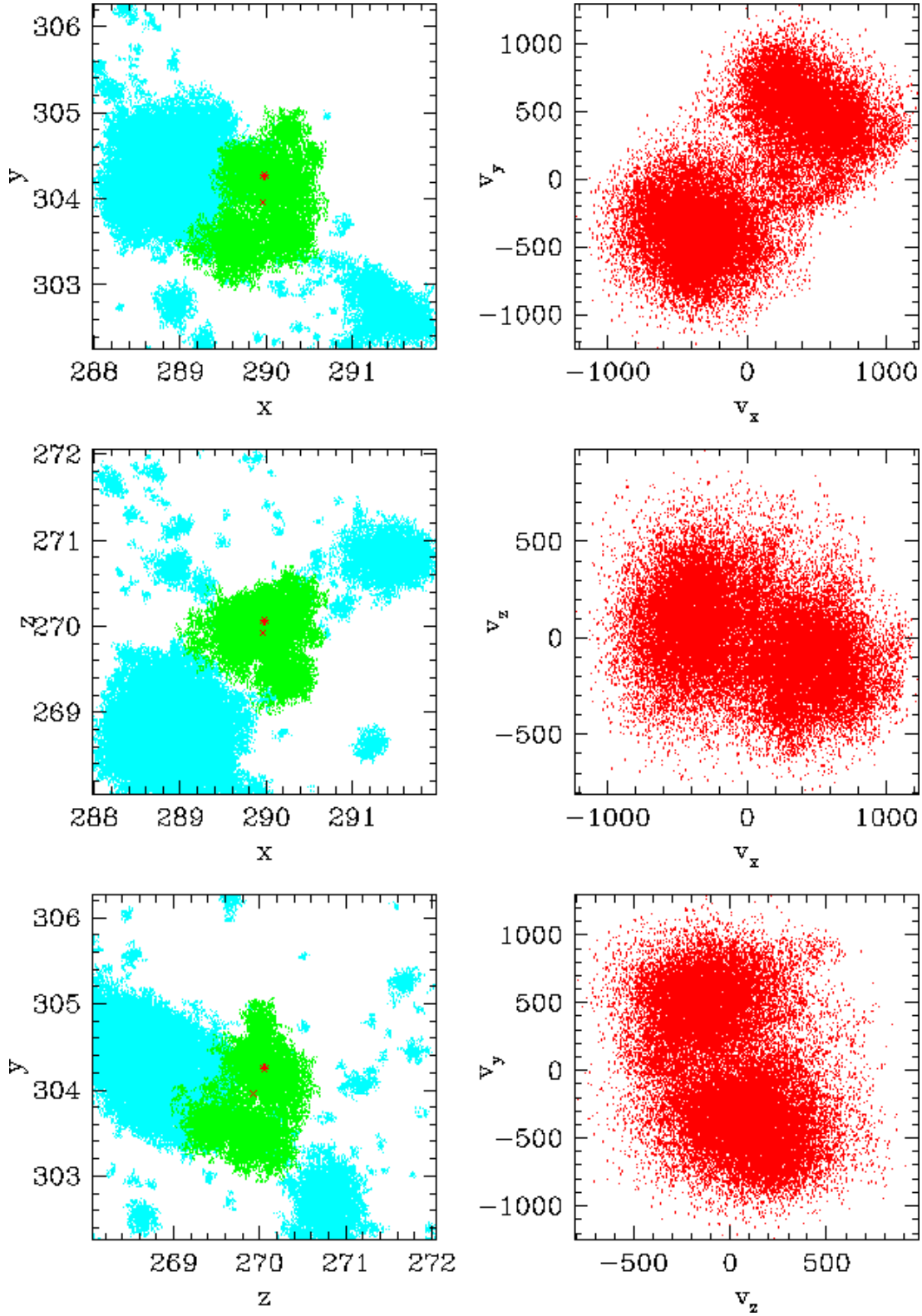


Figure A2. As Fig. A1, but showing an example of a larger multi-object FOF halo. This halo has a mass of $M_h = 38741m_p \approx 3.33 \times 10^{13} h^{-1} M_\odot$, and a spin parameter of $\lambda = 0.3295$. Its virial ratio, $\frac{2T}{U} + 1 = -2.05$ means it is excluded from the FOF-QE catalogue.

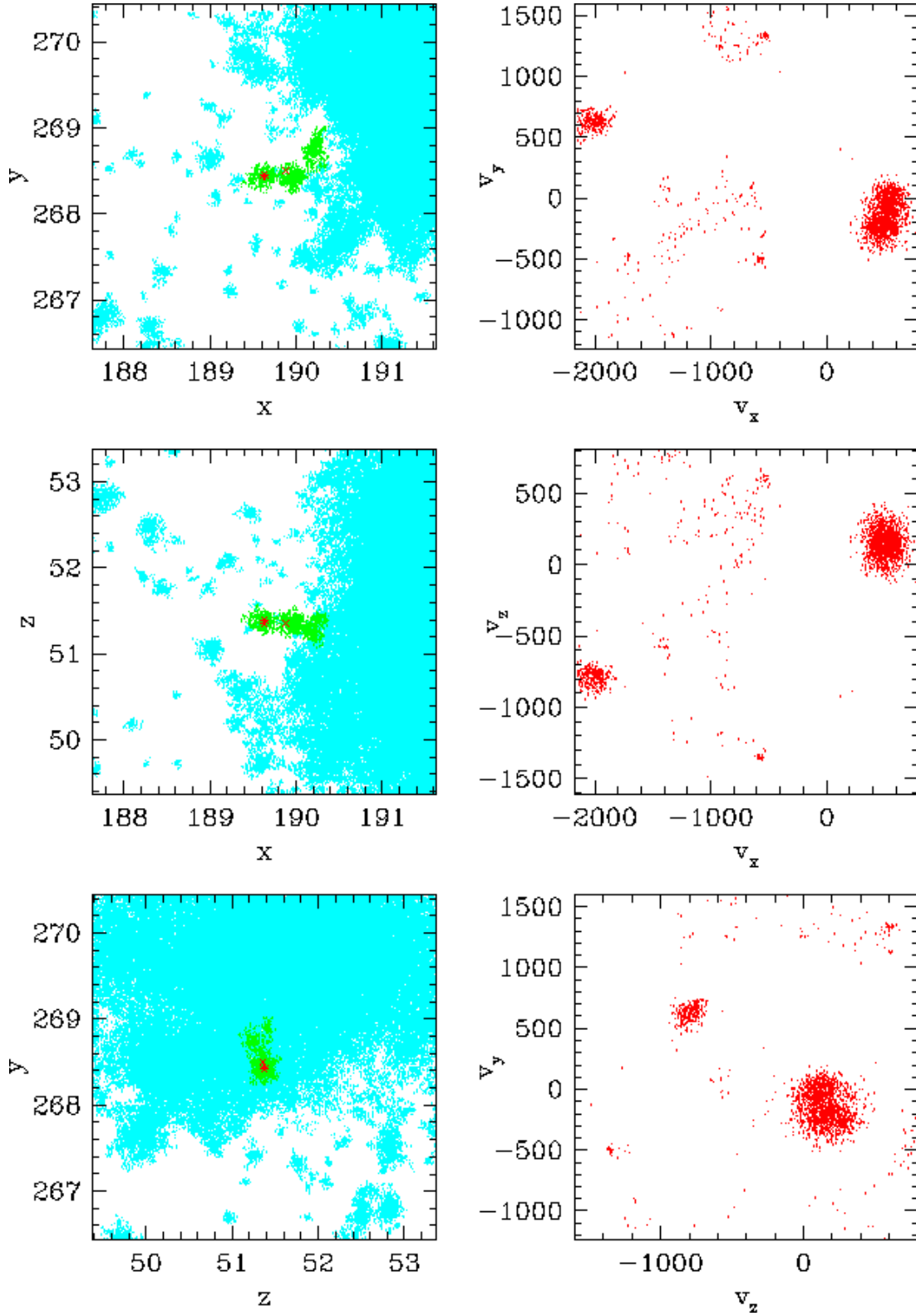


Figure A3. As Fig. A1, but showing an example of a small FOF halo with a large neighbour. The selected halo has a mass of $M_h = 1967m_p \approx 1.69 \times 10^{12} h^{-1} M_\odot$, and a spin parameter of $\lambda = 17.60$. Its virial ratio, $\frac{2T}{U} + 1 = -53.8$ means it is excluded from the FOF-QE catalogue.

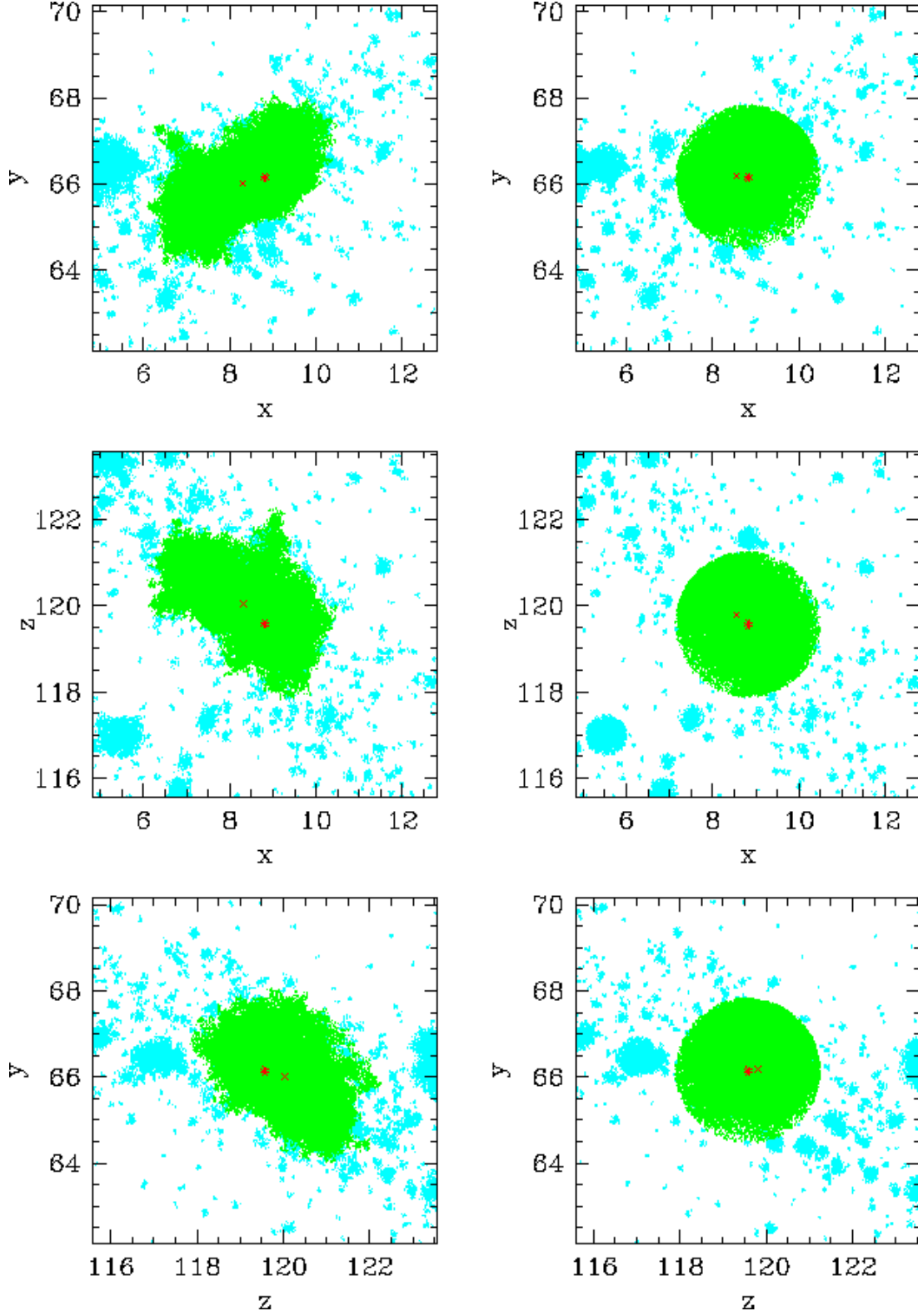


Figure A4. As Fig. A1, but showing a comparison of a FOF halo (left) and the corresponding SO halo (right), and their neighbours in each catalogue within $4 h^{-1}\text{Mpc}$. Only $1/4$ of the particles are plotted. Note how the SO halo includes particles that were not part of the FOF group, and are much less dense than the halo proper. The FOF halo has a mass of $M_h = 744\,019m_p \approx 6.40 \times 10^{14} h^{-1}M_\odot$, and a spin of $\lambda = 0.05959$. It has a virial ratio of $\frac{2T}{U} + 1 = -0.262$, so it is included in the FOF-QE catalogue. The SO halo has a mass of $M_h = 610\,023m_p \approx 5.25 \times 10^{14} h^{-1}M_\odot$, and a spin of $\lambda = 0.04539$. It has a virial ratio of $\frac{2T}{U} + 1 = -0.332$, slightly less relaxed than its FOF counterpart but still included in the SO-QE catalogue.

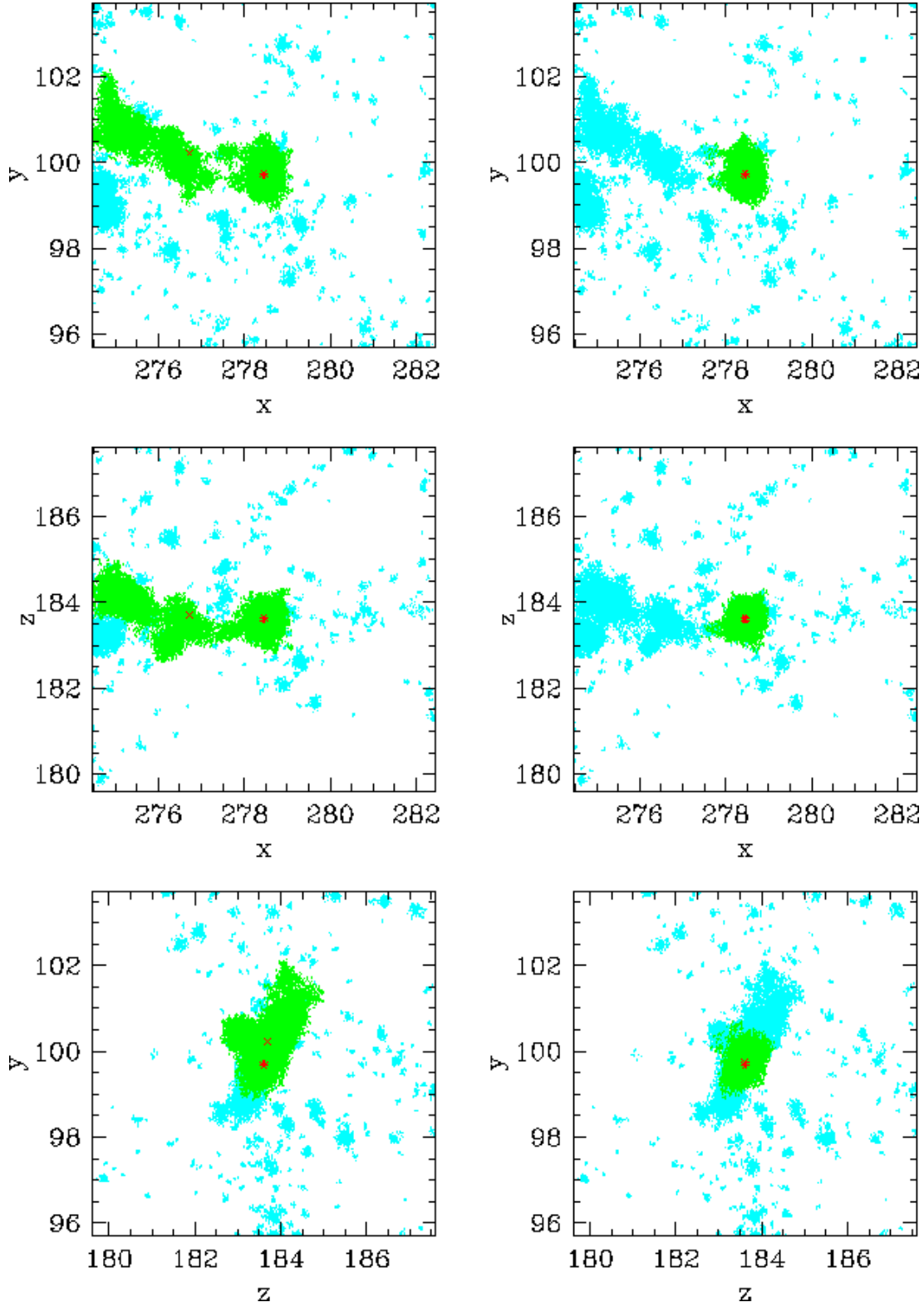


Figure A5. As Fig. A4, but comparing a FOF halo (left) and the corresponding TREE haloes (right). Only 1/4 of the points are plotted. Note how the FOF halo is highly extended, with the subhalo housing the potential minimum being linked to a large neighbouring halo. The TREE catalogue splits these into two objects. The FOF halo has a mass of $M_h = 126\,033m_p \approx 1.08 \times 10^{14} h^{-1} M_\odot$, and a spin of $\lambda = 0.1953$. It has a virial ratio of $\frac{2T}{U} + 1 = -0.111$, so it is included in the FOF-QE catalogue. The TREE halo has a much lower mass of $M_h = 40\,719m_p \approx 3.50 \times 10^{13} h^{-1} M_\odot$, and a spin of $\lambda = 0.05711$. It is slightly less relaxed however, with a virial ratio of $\frac{2T}{U} + 1 = -0.159$; it is included in the TREE-QE catalogue.